J. Fluid Mech. (1997), *vol.* 331, *pp.* 1–36

The effects of thermal conductivity and viscosity of argon on shock waves diffracting over rigid ramps

By L. F. HENDERSON[1]†, W. Y. CRUTCHFIELD[2] AND R. J. VIRGONA[3]‡

[1]IUSTI-MHEQ, Saint-Jérôme Centre, Université de Provence, 13397 Marseille, France
[2]Center for Computational Sciences and Engineering, Lawrence Berkeley National Laboratory, Berkeley, 94720 CA, USA
[3]Department of Mechanical Systems Engineering, Tokyo Noko University, Naka-Cho 2-24-16, Koganei, Tokyo 184, Japan

(Received 4 July 1995 and in revised form 19 August 1996)

Experiments were done with strong shocks diffracting over steel ramps immersed in argon. Numerical simulations of the experiments were done by integrating the Navier–Stokes equations with a higher-order Godunov finite difference numerical scheme using isothermal non-slip boundary conditions. Adiabatic, slip boundary conditions were also studied to simulate cavity-type diffractions. Some results from an Euler numerical scheme for an ideal gas are presented for comparison. When the ramp angle θ is small enough to cause Mach reflection MR, it is found that real gas effects delay its appearance and that the trajectory of its shock triple point is initially curved; it eventually becomes straight as the MR evolves into a self-similar system. The diffraction is a regular reflection RR in the delayed state, and this is subsequently swept away by a corner signal overtaking the RR and forcing the eruption of the Mach shock. The dynamic transition occurs at, or close to, the ideal gas detachment criterion θ_e. The passage of the corner signal is marked by large oscillations in the thickness of the viscous boundary layer. With increasing θ, the delay in the onset of MR is increased as the dynamic process slows. Once self-similarity is established the von Neumann criterion is supported. While the evidence for the von Neumann criterion is strong, it is not conclusive because of the numerical expense. The delayed transition causes some experimental data for the trajectory to be subject to a simple parallax error. The adiabatic, slip boundary condition for self-similar flow also supports the von Neumann criterion while $\theta < \theta_e$, but the trajectory angle discontinuously changes to zero at θ_e, so that θ_e is supported by the numerics, contrary to experiments.

1. Introduction

Consider the regular and irregular wave systems which appear when a plane incident shock i diffracts over a rigid ramp of apex angle θ as in figure 1. In this paper a detailed study is made of the transition between regular (RR, figure 1*a*)

† Permanent address: 8 Damour Avenue, East Lindfield, Sydney NSW 2070, Australia.
‡ Current address: Sirindhorn International Institute of Technology, Thammasat University, Thailand

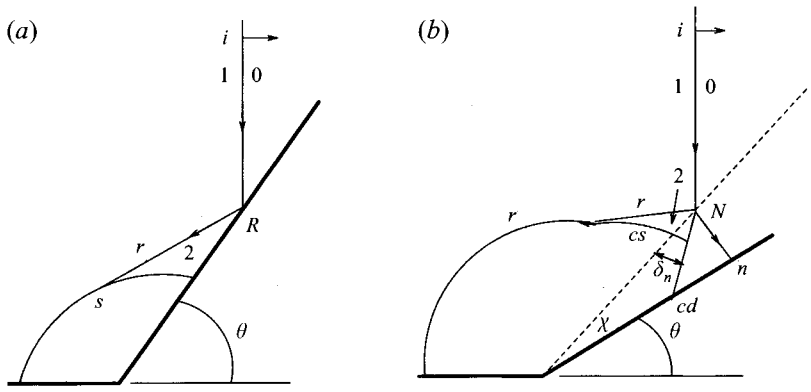

FIGURE 1. Regular and irregular strong shock diffraction. (*a*) RR; (*b*) CMR; states *i*, incident shock; *r*, reflected shock; *n*, Mach shock; *cs*, corner signal; *r'*, augmented reflected shock; *cd*, contact discontinuity; *B*, interaction zone; *N*, triple point node; *R*, RR node; θ, ramp angle; χ, triple point trajectory angle; δ_n, particle path deflection across *n* shock; η, ramp impact angle; subscripts: 0, undisturbed state; 1,2, states downstream of *i* and *r*, respectively.

and irregular (IR) reflection on the ramp. Here the IR will be either a self-similar complex Mach reflection (CMR, figure 1*b*), or a non-steady system of somewhat similar appearance. As usual, *i* is defined to be strong if near transition RR $\rightleftharpoons$ IR, the flow leaving the reflected shock is supersonic $M_2 > 1$, where M is the flow Mach number for coordinates that are fixed with respect to either the reflection node R, or the Mach (shock triple point) node N, and states 0, 1, and 2 are indicated in figure 1. Conversely, *i* is weak when $M_2 < 1$. Irregular systems have different structures in the strong and weak cases. The weak irregularities include single Mach reflection (SMR) and von Neumann reflection (VNR). A CMR or double Mach reflection (DMR) is impossible for stationary and pseudo-stationary weak shocks because the necessary condition that $M_2 > 1$ is not fulfilled. However a CMR or DMR appears possible when the system is neither stationary or pseudo-stationary, such as when either a corner signal or a shock overtakes a SMR from the rear.

The transition criteria which determines when RR $\rightleftharpoons$ IR have been discussed previously for the perfect gas (Henderson 1987; von Neumann 1963; Hornung 1986; Ben-Dor 1992). There are three alternative criteria for strong shock transition, namely the detachment point θ_e (von Neumann 1963), the sonic point θ_s (Hornung, Oertel & Sandeman 1979; Lock & Dewey 1989), and the von Neumann point θ_N (von Neumann 1963; Henderson & Lozzi 1975). The angles θ_e and θ_s are very close and it is usually difficult to discriminate between them, but the θ_N point is sufficiently different from the others to be discriminated experimentally.

Many experimenters have found that the θ_N point correctly predicts transition for stationary shock systems, as in a wind tunnel (Hornung, Oertel & Sandeman 1979; Henderson & Lozzi 1975; Mölder 1971; Pantazapol, Bellet & Soustre 1972; Hornung & Robinson 1982). However, transition may be forced to other positions by changing the system boundaries, such as by using cylindrical instead of plane surfaces (Heilig 1969; Henderson & Lozzi 1979; Ben-Dor 1992); hysteresis effects may also be observed. Stationary and symmetric boundaries are illustrated in figure 2(*a*). Although the data are more scattered, there is also evidence that the θ_N point is correct for the unsteady self-similar symmetric internal cavity diffractions, shown in figure 2(*b*), (Henderson & Lozzi 1975, 1979). By contrast, for the asymmetric, but unsteady, self-similar diffraction over ramp, figure 2(*c*), transition occurs closest to

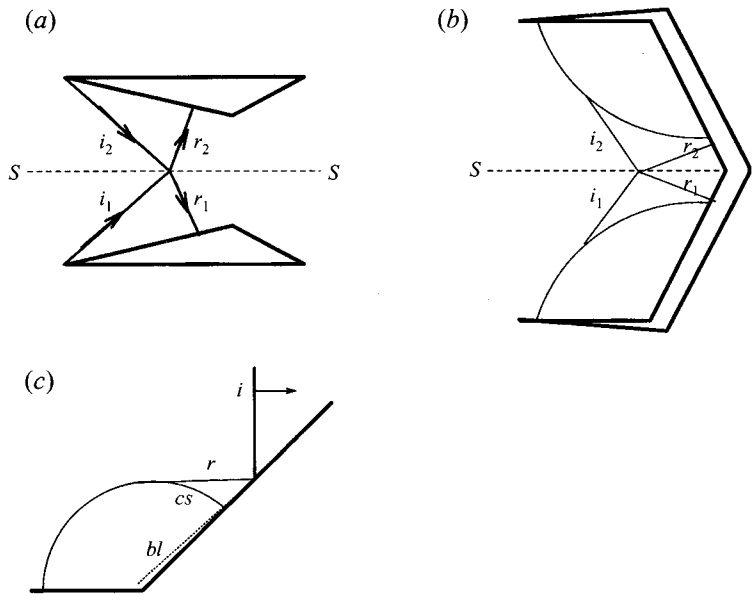

FIGURE 2. Symmetrical and unsymmetrical shock reflection: (*a*) stationary, symmetrical reflection; (*b*) self-similar, symmetrical reflection; (*c*) self-similar unsymmetrical reflection with a boundary layer.

the θ_e point. The experiments often show that RR persists for conditions that should make its existence impossible according to the von Neumann theory for a perfect gas (Henderson & Lozzi 1975, 1979; Bleakney & Taub 1949; Kawamura & Saito 1956; Hornung 1986). Thus the θ_e point is not an accurate criterion in this case, and this effect is referred to as the von Neumann paradox. It has long been recognized that viscosity and thermal conductivity could affect the transition. For example, a boundary layer begins at the reflection point on the ramp surface in figure 2(*c*), and the slope of its displacement height at this point could affect transition. But there is no boundary layer at the reflection point of any of figure 2(*a,b*), because those occur on planes of symmetry, and not on physical surfaces.

The present paper presents a study of the diffraction of a strong shock over a ramp in a real gas. A real gas is defined as one which has a finite shear viscosity μ and thermal conductivity k. The object is to find what effects these properties have on the diffractions and on their transition. It is found that the real gas properties delay the onset of MR on the ramp, and delay its evolution to a self-similar state. Our studies contrast the effects of two different boundary conditions on the ramp. One boundary condition corresponds to the existence of a boundary layer on the ramp, while the other corresponds to shock reflection at a plane of symmetry where there is no boundary layer even in a real gas. For the latter boundary condition there is typically no delay in the onset of MR and self-similarity is attained rapidly when $\theta < \theta_e$ and θ is not too close to θ_e. But when $\theta \to \theta_e$ from below, an MR is still obtained but its evolution to self-similarity is increasingly delayed. It is found that both the θ_e point and the θ_N points are important in strong shock diffraction, but that the two angles control different aspects of the diffraction. We also take the opportunity to study the effect of other boundary conditions on the ramp surface upon the shock system.

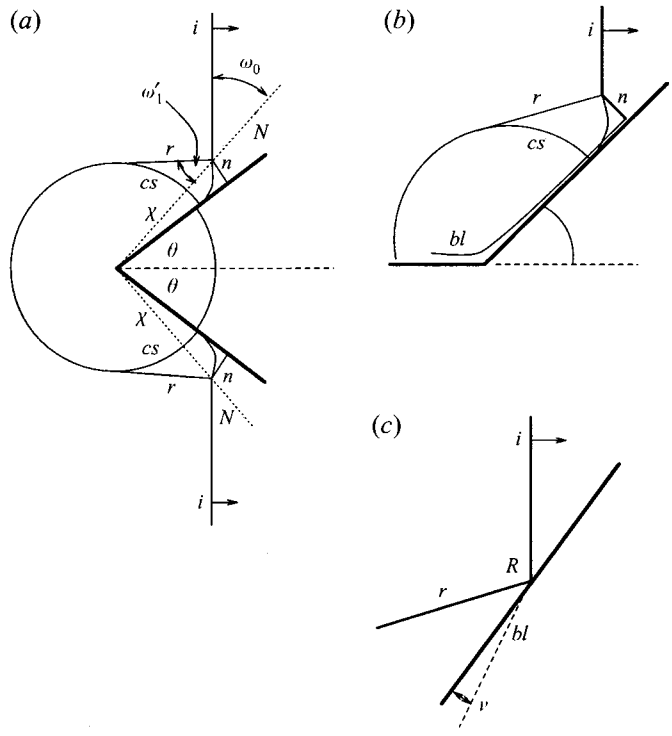

FIGURE 3. Model designs for shock diffraction experiments: (*a*) symmetrical model (*b*) concave corner model (*c*) boundary layer (bl) in node fixed coordinates; v, boundary layer deflection angle at node R, ω_0, ω_1', wave angles of i and r with respect to the triple point trajectory.

The methods employed for the investigation were shock tube experiments and numerical simulation of them by integration of the unsteady Navier–Stokes equations. Some numerical results for an inviscid, non-heat conducting perfect gas are presented for comparison.

2. The experiments

These were done in a conventional shock tube and are fully described elsewhere (Virgona 1993). Some of the data will be presented below. The shocks propagated in argon, which was chosen to simplify the physics. For example, there was no molecular vibration, rotation, dissociation, or bulk viscosity and for the shock Mach number of the experiments $M_i = 2.33$ there was no electron excitation or ionization. The significant non-ideal gas effects were caused by the shear viscosity and thermal conductivity.

Strong plane shock waves were diffracted over smooth solid steel symmetrical ramp models of various semi-apex angles θ, see figure 3(*a*). This design was chosen to reduce shock-boundary layer interactions which can be a troublesome aspect of concave corner models, see figure 3(*b*).

We measured the angle χ between the trajectory and the ramp surface, see figure 3(*a*). This was done by taking a schlieren photograph of the diffraction after the shock had progressed approximately 4 cm up the ramp. In order to tie the measured angle χ with the physical evolution of the shock diffraction, we must assume that the Mach shock n and indeed the whole system grows uniformly in time t; in other

words, the system is self-similar. The assumption is called the *parallax assumption* and since it is of some importance, it is stated formally. We emphasize that this is an assumption and will later present evidence that the assumption is sometimes incorrect.

Parallax assumption. A Mach reflection (SMR, CMR, DMR) present in the diffraction of a plane shock over a rigid plane ramp always grows self-similarly with time. In particular, the trajectory of its shock triple point is a straight line which always passes through the apex (corner) of the ramp.

3. The gas model

The minimum undisturbed pressure of the argon was about 0.1 atmosphere, while the maximum pressure caused by the shock compression was about 4 atmospheres. The minimum temperature of the undisturbed argon was about 288 K during the experiments, while the maximum temperature of the shock compressed gas was about 1400 K. In the numerical computations, we have represented the argon as a continuous medium because the mean free path is less than any discretization scales Δx.

For these states, it was assumed that the virial equation of state applied,

$$Z = \frac{pv}{RT} = 1 + \frac{B(T)}{v} + \cdots, \tag{1}$$

where Z is the compressibility factor and B is the first virial coefficient. The gas tables of Hilsenrath *et al.* (1960) were used to find Z for the p and T ranges of interest,

$$p = 0.1 \text{ atm}, \ 290 \leqslant T \leqslant 1400 \text{ K} \rightarrow 0.9993 \leqslant Z \leqslant 1.00002, \tag{2}$$

$$p = 4.0 \text{ atm}, \ 290 \leqslant T \leqslant 1400 \text{ K} \rightarrow 0.99705 \leqslant Z \leqslant 1.00085. \tag{3}$$

so the error is less than 1% if argon is assumed to obey the perfect gas equation of state. The variation in the ratio of the specific heats is small, $\gamma = 5/3 \pm 0.014$ for these ranges. We used the constant value $\gamma = 5/3$.

For the viscosity μ we assumed that

$$\mu = \frac{2.01572 \times 10^{-6} \ T^{1.5}}{171.691 + T} \text{kg m}^{-1}\text{s}^{-1} . \tag{4}$$

This functional form was determined by fitting a curve to the tables and is accurate to better than 1% in the given temperature range. To the same accuracy in this temperature range, the Prandtl number P_r for argon is 0.67,

$$P_r = \frac{\mu C_p}{k} , \tag{5}$$

where C_p is the specific heat at constant pressure and k is the thermal conductivity. The thermal conductivity k can then be found from the Prandtl number P_r. The coefficient of second viscosity λ is taken to be $-2/3\mu$ as is appropriate for argon.

4. The computations

4.1. *Plan*

The computations were planned as though we were doing experiments in a shock tube. The following quantities were held constant:

$$\gamma = \tfrac{5}{3}; \quad P_r = 0.67; \quad p_0 = 14.1 \text{ kPa}; \quad T_0 = 293.15 \text{ K} \tag{6}$$

θ_e	θ_s	θ_N
53.776	53.924	57.021

TABLE 1. Transition criteria for $\gamma = 5/3$, $M_i = 2.327$. θ_e detachment criterion; θ_s sonic criterion; θ_N von Neumann criterion.

where the subscript refers to conditions in the undisturbed gas, and T_0 is also the temperature of the ramp which was assumed to be isothermal. A method in Mark (1958) was used to check the assumption that the ramp surface is isothermal. By this means, the temperature rise caused by the passage of the shock was estimated to be $O(10^{-3})$ K, so the error is small.

The incident shock Mach number was also constant $M_i = 2.327$, which ensured that i was always a strong shock. The ramp angle θ was variable and its values were selected to explore the effects of viscosity and thermal conductivity on transition. The values of θ were chosen to cover the neighbourhood of the alternative transition angles, see table 1.

4.2. *Formulation*

The compressible Navier–Stokes equations for two-dimensional viscous unsteady polytropic gas dynamics are a mixed set of hyperbolic-parabolic partial differential equations which may be written in conservation form as (Anderson, Tannehill & Pletcher 1984)

$$\partial_t \boldsymbol{U} + \boldsymbol{F}(\boldsymbol{U})_x + \boldsymbol{G}(\boldsymbol{U})_y = \boldsymbol{R}(\boldsymbol{U})_x + \boldsymbol{S}(\boldsymbol{U})_y \tag{7}$$

where

$$\boldsymbol{U} = \begin{pmatrix} \rho \\ \rho u \\ \rho v \\ \rho E \end{pmatrix}, \tag{8}$$

$$\boldsymbol{F}(\boldsymbol{U}) = \begin{pmatrix} \rho u \\ \rho u^2 + p \\ \rho uv \\ u(\rho E + p) \end{pmatrix}, \tag{9}$$

$$\boldsymbol{G}(\boldsymbol{U}) = \begin{pmatrix} \rho v \\ \rho uv \\ \rho v^2 + p \\ v(\rho E + p) \end{pmatrix}, \tag{10}$$

$$\boldsymbol{R}(\boldsymbol{U}) = \begin{pmatrix} 0 \\ (\lambda + 2\mu)u_x + \lambda v_y \\ \mu(u_y + v_x) \\ uR_2 + vR_3 + (\mu/P_r)\gamma e_x \end{pmatrix}, \tag{11}$$

$$\boldsymbol{S}(\boldsymbol{U}) = \begin{pmatrix} 0 \\ \mu(u_y + v_x) \\ (\lambda + 2\mu)v_y + \lambda u_x \\ uS_2 + vS_3 + (\mu/P_r)\gamma e_y \end{pmatrix}, \tag{12}$$

$$e = E - (u^2 + v^2)/2 \tag{13}$$

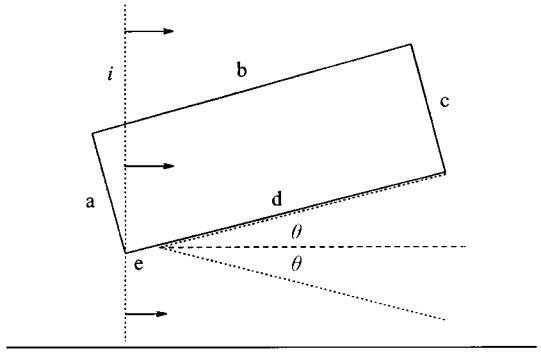

FIGURE 4. The rectangular computational domain is aligned with the top surface of the wedge. The boundary conditions on the boundary segments a–e are described in the text.

As usual, ρ is density, u and v are the x and y velocity components respectively, E is the specific energy, e is the specific internal energy, subscripting by x or y indicates a derivative, and subscripting by 2 or 3 indicates the second or third component of a vector. These equations include the viscous transport of momentum, diffusive transport of heat energy, and the dissipation of kinetic energy into heat. In the simulations, we assume that argon is well described by the perfect gas law,

$$p = \rho RT \ . \tag{14}$$

When combined with (13), the perfect gas law implies

$$p = (\gamma - 1)\rho \left(e - \tfrac{1}{2}\left(u^2 + v^2\right)\right). \tag{15}$$

The computational domain is taken to be a rectangle whose lower edge is aligned with the surface of the ramp, as in figure 4. For the coordinate system which is aligned with the computational domain, the surface of the ramp is at $y = 0$. The component u is tangential to the surface of the ramp, while the component v is normal. An incident shock i enters computational domain from the left at an oblique angle to the computational domain. There are five different boundary conditions on the computational domain. On edge a, the boundary condition is supersonic inflow of the post-shocked state. The boundary condition on edge b is a sharp transition between post- and pre-shocked states which moves to the right at the speed of the shock. On edge c, the boundary condition is that of the pre-shocked state. On the segment e, the boundary condition requires outflow.

Segment d, where the boundary is coincident with the surface of the ramp, is of particular interest. The ramp surface is taken to be isothermal with a temperature $T = 293.15$ K. The ramp surface is also taken to be non-slip, with tangential component $u = 0$.

4.3. *The algorithm*

The computations described in this paper employ an adaptive semi-implicit scheme appropriate for unsteady viscous compressible flow (Steinthorsson, Modiano & Colella 1994; Steinthorsson *et al.* 1995). The algorithm has two important components: the semi-implicit finite difference scheme and the adaptive mesh refinement (AMR) implementation of the scheme. We will describe the finite difference scheme first.

This finite difference scheme employs a predictor-corrector cycle, combining an explicit higher-order Godunov prediction of the hyperbolic fluxes at a half-time level with an implicit Crank–Nicolson correction. Note that the scheme employs cells with an aspect ratio of one. The entire scheme is second-order accurate in time and space for smooth flows. In analogy to Godunov schemes for the Euler equations, the scheme is first-order accurate in the presence of an unresolved discontinuity, i.e. shock or contact discontinuity. In the predictor step of the algorithm, we use a straightforward extension of the unsplit second-order Godunov integration algorithm of Colella (1990) to compute the fluxes $F^{n+1/2}$ and $G^{n+1/2}$ at the half-time level. In the computation of $F^{n+1/2}$ and $G^{n+1/2}$, the viscous fluxes enter only as sources computed at the lagged time level, R^n and S^n. The lagging of the viscous flux source terms makes the Godunov fluxes $F^{n+1/2}$ and $G^{n+1/2}$ only first-order accurate. However, the order of the finite difference method may be raised to second order by employing a Crank–Nicolson correction:

$$\begin{aligned} U_{i,j}^{n+1} = U_{i,j}^{n} &+ \frac{\Delta t}{\Delta x}(F_{i-1/2,j}^{n+1/2} - F_{i+1/2,j}^{n+1/2}) + \frac{\Delta t}{\Delta y}(G_{i,j-1/2}^{n+1/2} - G_{i,j+1/2}^{n+1/2}) \\ &+ \frac{\Delta t}{2\Delta x}(R_{i+1/2,j}^{n} - R_{i-1/2,j}^{n}) + \frac{\Delta t}{2\Delta y}(S_{i,j+1/2}^{n} - S_{i,j-1/2}^{n}) \\ &+ \frac{\Delta t}{2\Delta x}(R_{i+1/2,j}^{n+1} - R_{i-1/2,j}^{n+1}) + \frac{\Delta t}{2\Delta y}(S_{i,j+1/2}^{n+1} - S_{i,j-1/2}^{n+1}). \end{aligned} \tag{16}$$

Equation (16) is an implicit equation for U^{n+1} because R^{n+1} and S^{n+1} are functions of the variable U at the $(n+1)$th time level. In the work described in this paper, the implicit equations were solved with a Gauss–Seidel relaxation.

The shock diffraction problem has a very large range of length scales. The length scale of the experimental apparatus which is being simulated is the order of several centimetres. The viscous boundary layer which forms on the ramp surface behind the incident shock has a thickness measured in microns. The thickness of the boundary layer approaches zero as the shock is approached. Resolving both of these length scales with a single uniform grid would require a prohibitive amount of computational resources. For these reasons, an adaptive numerical method is required which concentrates computational effort into small regions which require high accuracy and high resolution. The adaptive method described in this paper is based on a hierarchical grid approach first developed by Berger & Oliger (1984) for hyperbolic partial differential equations. This approach has been demonstrated to be highly successful in two dimensions for high-speed flow (Berger & Colella 1989) and in three dimensions (Bell *et al.* 1994). An extension of this methodology to the incompressible Euler equations is described in Almgren *et al.* (1993). AMR is based on a sequence of nested grids with successively finer spacing in both time and space. These fine grids are recursively embedded in coarser grids until the solution is sufficiently resolved. An error estimation procedure automatically gauges the accuracy of the solution and grid generation procedures dynamically create or remove rectangular fine grid patches as resolution requirements change.

Figure 5, reproduced from Pember *et al.* (1995), demonstrates the hierarchical grid structure in an application of AMR to inviscid gas dynamics. The contours in figure 5 indicate increasing density in the interaction of a shock with an inclined ramp. Each rectangular box in the figure indicates an individual grid in a hierarchy of nested grids. The rectangle enclosing the entire problem domain is the single grid at the coarsest level of refinement. At the next finest level of refinement, a set of grids covers

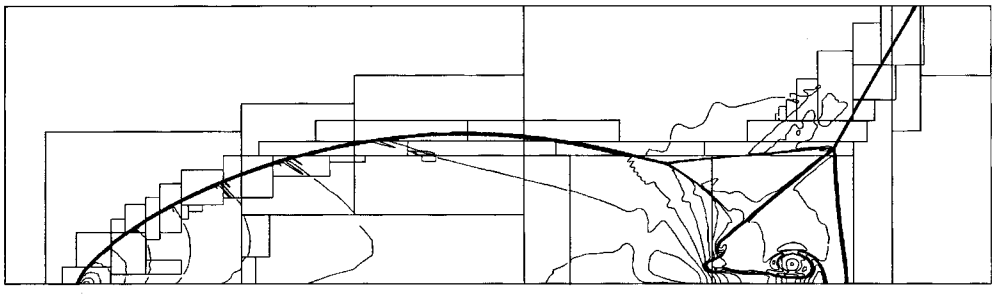

FIGURE 5. Application of hyperbolic AMR for inviscid compressible gas dynamics in the interaction of a shock and an inclined ramp using three levels of refinement. Rectangles are grids used in the adaptive gridding strategy. Contours indicate density. Note that grids on finer levels of refinement are automatically placed on regions of large gradients in the solution.

the interaction region with higher resolution. A third and finest level of refinement is shown in the figure as relatively small boxes. Note that the grids on this finest level of refinement are concentrated in regions of large gradients in the solution. This is the result of an automatic adaptation of the grids to the changing solution.

Rather than describe the AMR algorithm for the compressible Navier–Stokes equations in full detail (see Steinthorsson *et al.* 1994, 1995), we will briefly describe how it differs from an AMR algorithm for a purely hyperbolic equation (Berger & Oliger 1984; Berger & Colella 1989; Bell *et al.* 1994). AMR for hyperbolic systems uses a purely explicit time-stepping method. The basic discretization method for compressible Navier–Stokes equations described above has both an explicit prediction step and an implicit correction step. The compressible Navier–Stokes AMR algorithm therefore solves an implicit equation during the time-step advance, unlike the hyperbolic AMR algorithm.

In AMR, coarse and fine grids are advanced in time at different speeds. However, the time steps are chosen such that a finer level of refinement synchronizes with a coarser level after a small integer number of time steps. In general, coarse grid cells are updated using fluxes computed on the coarse grid and fine grid cells are updated using fluxes computed on the fine grid. However, this prescription is inadequate for coarse grid cells directly adjoining a fine grid because on the shared face both coarse and fine grid fluxes are available. In order to preserve strict conservation and accuracy, it is desirable to update such coarse grid cells using the available fine grid fluxes, summed over the appropriate number of fine grid time steps. This is performed as a correction step: (i) the coarse cell is updated with coarse grid fluxes, (ii) the fine grids make sufficient time steps to reach the coarse grid time, accumulating fluxes on the coarse–fine boundary, (iii) the coarse cell is updated with the difference between the coarse grid flux and the summed fine grid fluxes.

This adjustment to the coarse grid flux is performed in both the hyperbolic AMR algorithm and the compressible Navier–Stokes algorithm. The two AMR algorithms differ in their definition of the flux. For hyperbolic AMR, the flux is the Godunov flux, while for the compressible Navier–Stokes algorithm, the flux is an appropriately time-centred sum of Godunov fluxes and viscous fluxes, i.e.

$$F^{n+1/2} \rightarrow F^{n+1/2} + \frac{R^n + R^{n+1}}{2}. \tag{17}$$

Note that for the compressible Navier-Stokes AMR algorithm, both the coarse and fine grid fluxes are computed implicitly, but the update to the adjacent coarse cells

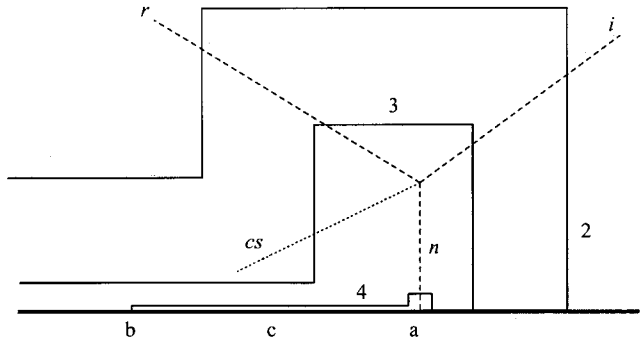

FIGURE 6. Typical levels of refinement around Mach reflection pattern. Dashed lines indicate incident shock *i*, reflected shock *r*, Mach stem *n*. Dotted line is contact surface *cs*. Solid lines show boundaries of refinement regions 2, 3, and 4. Refinement regions 0 and 1 are not shown.

is performed explicitly. In comparison, a more complex consistency scheme between different levels of refinement is imposed in the AMR algorithm for the incompressible Euler equations (Almgren *et al.* 1993).

The algorithm described in this paper and in Steinthorsson *et al.* (1994, 1995) was implemented using mixed language programming, i.e. the organizational levels of AMR were written in the C++ programming language while all routines performing floating point intensive parts of the algorithm (e.g. the Godunov integrator and linear algebra solvers) were written in FORTRAN. The AMR C++ class structure for this algorithm is described in Crutchfield & Welcome (1993).

4.4. *Regridding strategy*

Adaptive mesh refinement algorithms must specify the policy by which fine grids are recursively allocated on the problem domain. The compressible Navier–Stokes AMR algorithm uses a combination of two mechanisms. The first mechanism automatically tags cells as requiring further refinement if a Richardson extrapolation of the solution on two different levels of refinement indicates that additional refinement is necessary to maintain a given level of accuracy (Berger & Colella 1989). A second mechanism allows the user to manually override the automatic error estimation and mark certain regions as either never requiring refinement or always requiring refinement. The second mechanism is implemented as a user-defined subroutine which is executed after the automatic mechanism has computed error estimates for the cells. The second mechanism would be employed when the user has knowledge of the physical problem that provides a more accurate specification of where refinement is required.

For the purposes of this paper, it is a practical necessity to manually override the automatic placement of grids. Given the extreme range of scales to be resolved, it is necessary to reduce the size of the refined regions to a practical minimum. Here, we are concerned with the effect of viscosity upon the shock reflection pattern. The finest-scale viscous structures will form in regions of maximum velocity and temperature gradients. One such region considered to have physical importance is at the surface of the ramp. Therefore in this paper, the finest grids are concentrated at the surface of the ramp. In addition, preliminary calculations have shown the existence of a strong rarefaction fan where the Mach stem intersects the ramp surface. Therefore, refinement will also be allowed in a rectangular region surrounding the point at the surface which intersects either the Mach stem (Mach reflection) or the initial shock

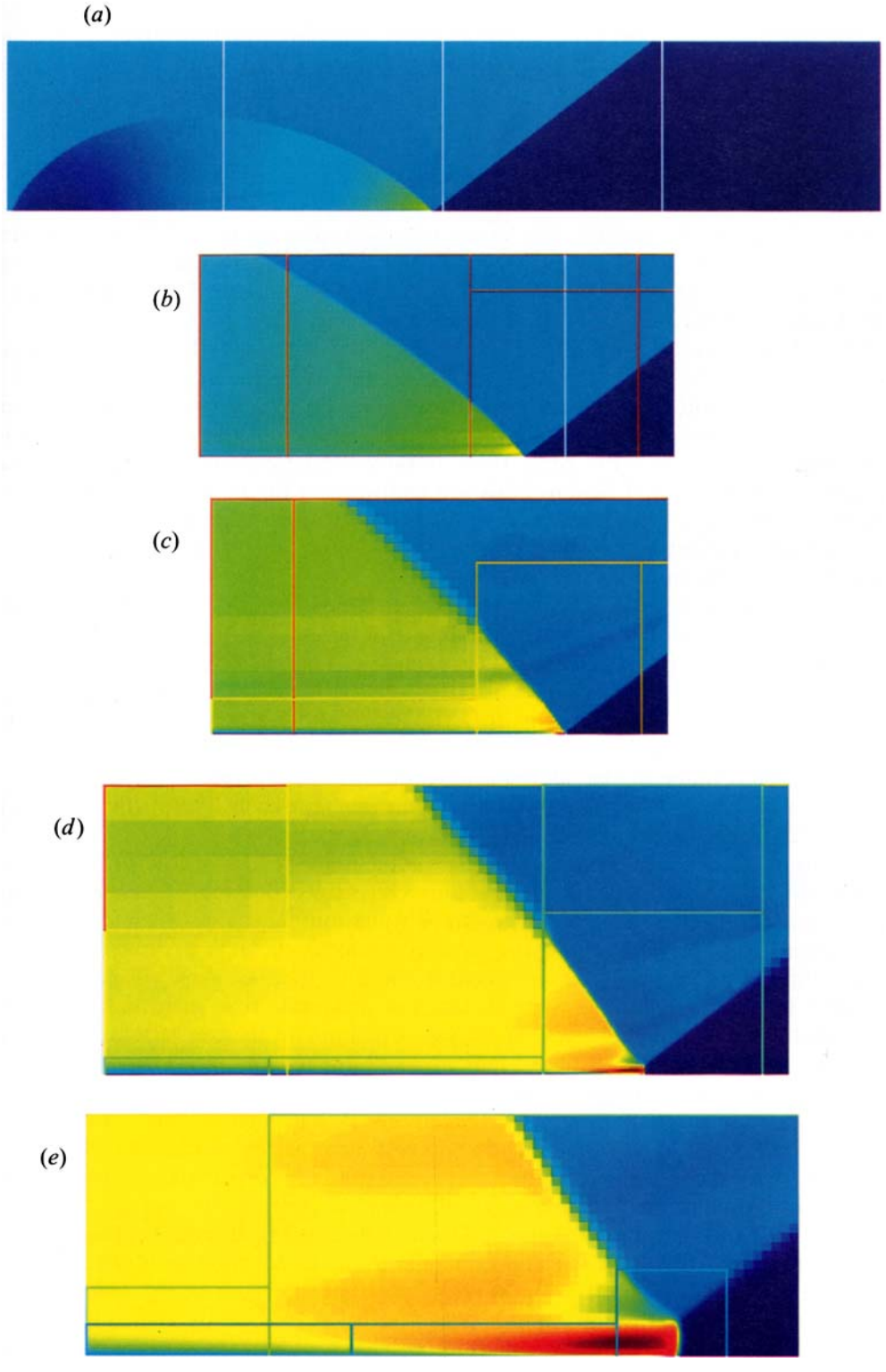

FIGURE 7. Five levels of refinement in a compressible Navier–Stokes calculation. The coarsest level is (*a*). Each succeeding level (*b–e*) is refined by factor of four.

Level	0	1	2	3	4
Δx (m)	1.0×10^{-4}	2.6×10^{-5}	6.5×10^{-6}	1.6×10^{-6}	4.1×10^{-7}
% refined	100	62	0.58	0.019	0.000374

TABLE 2. Percentage of computational domain which is refined at each level in typical calculation

(regular reflection). In general, shocks are not resolved to the finest level of refinement in this problem except when they fall within the regions described above, even though they have very large gradients. Even where shocks are covered by finest level grids, the shocks are not resolved by the grid, i.e. $\Delta x_4 \gg$ mean free path.

The calculations described utilize five levels of refinement, with each level a factor of four more refined than the next coarser level. The cell size of the nth level of refinement is denoted Δx_n. The levels are numbered from 0 to 4. On levels 0 and 1, only the automatic strategy is employed to place grids. Since coarse grids employ very little storage and CPU time, there is no reason to attempt to optimize their placement. On levels 2, 3, and 4, grids are restricted in the manner described above. Figure 6 illustrates a typical placement of the refined levels. The position of the grids is recalculated periodically, so the refined regions approximately retain these positions with respect to the moving shock waves.

Figure 7 illustrates the multilevel nature of AMR and the regridding strategy employed in this paper. Figure 7(*a*) is the coarsest level of refinement. Each succeeding level of refinement is a factor of four finer in resolution. Rectangular outlines in figure 7 indicate the location of refined regions as described above. At the coarsest level of refinement, neither the Mach shock nor the boundary layer is visible. The finest level of refinement clearly shows both features. In figure 7 only a very small percentage of the computational domain is resolved at the finest level of refinement. Table 2 show percentages of refinement for each level in the simulation for $\theta = 52°$ near the end of the calculation.

The approach described above introduces some numerical error into the simulation. Numerical error is introduced where a shock crosses a boundary between fine and coarse grids. Close examination of figure 7 will show faint smears emanating from such points. In regions where the flow is smooth, there is no detectable error emanating from boundaries between coarse and fine grids. Because we cannot afford to refine the entire length of every shock, it is inevitable that such numerical error exists in the calculation. Given that we cannot eliminate these errors, we have tried to minimize their effect upon important physical phenomena in shock diffraction by varying the size of the refined region. The dimensions of the refined regions shown in figure 6 have been set empirically. Our approach has been to repeat a calculation while increasing the size of the refined regions. When the results cease to change with increasing size of the refined regions, we choose that size for subsequent calculations.

We also employ the following rules of thumb in setting the size of the refined regions. First, if the solution forms a Mach stem, the Mach stem is always refined at least to level 3 (level 4 is the finest). The base of the Mach stem is always refined to the finest level. Second, the thickness of the refined region in the long flat layer extending far behind the initiating shocks is always 16 cells on the fourth (finest) level of refinement. On the third level of refinement, the layer beginning at c and extending off the figure is at least twice as thick as the grids of the fourth level that it encloses. Thirdly, the flat refinement layer is extended behind the initiating shock to

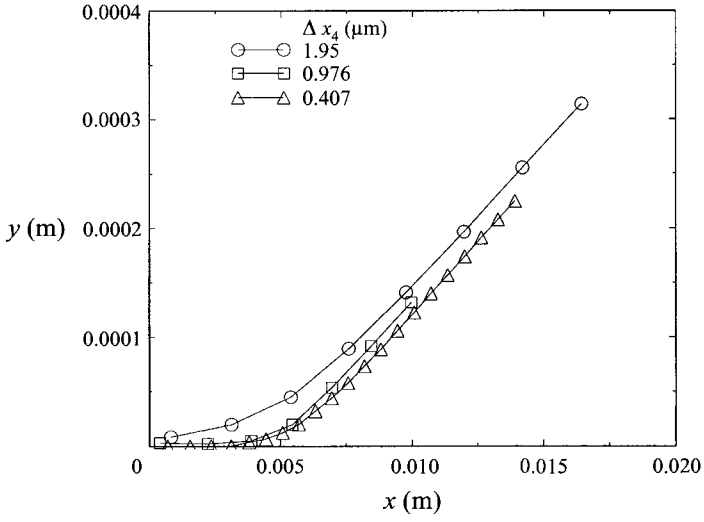

FIGURE 8. Triple-point trajectories at $\theta = 50.5°$ for varying resolutions Δx_4.

a distance at which the thickness of the viscous boundary layer becomes comparable to the thickness of the layer. At that point, the boundary layer is thick enough to be resolved on a next coarser level of refinement. That is the criterion by which the position b on the fourth level of refinement was chosen.

4.5. *Convergence studies*

In the problem of strong shock diffraction of real gases over a ramp, it is necessary to resolve very small scales, i.e. the boundary layer which forms at the surface of the ramp. It is well known (Mirels 1956; Mirels & Hamman 1962) that the boundary layer thins as the shock is approached from downstream and approaches zero thickness at the shock. It is therefore impossible with current computational resources to resolve the boundary layer in the immediate neighbourhood of the shock. This section will present evidence that it is possible to resolve enough of the important physical phenomena in this problem to make meaningful predictions.

One of the major results that this paper presents is that, unlike the Euler equation, the numerical solutions to compressible Navier–Stokes equations do not evolve in a self-similar manner. In particular, the trajectories of the shock triple point are not straight lines, but are curved. We also observe, as expected, that the trajectory depends strongly on the fine-grid resolution Δx, see figure 8. It is convenient to extract a single number from each trajectory to characterize its dependence upon grid resolution. Figure 9 shows how we analyse a shock triple-point trajectory in the (x, y)-plane and extract (among others) the quantity we denote as x_{int}, which is done by determining the line to which the trajectory asymptotes when it reaches self-similarity. The x intercept of that line is x_{int}.

Figure 10 shows the behaviour of x_{int} at $\theta = 50.5°$ as the finest grid resolution Δx_4 is decreased. This graph strongly suggests that x_{int} is converging to a finite value as $\Delta x_4 \to 0$ and that the order of convergence is first. This result is expected since, as stated earlier, the finite difference scheme is second-order accurate in regions of

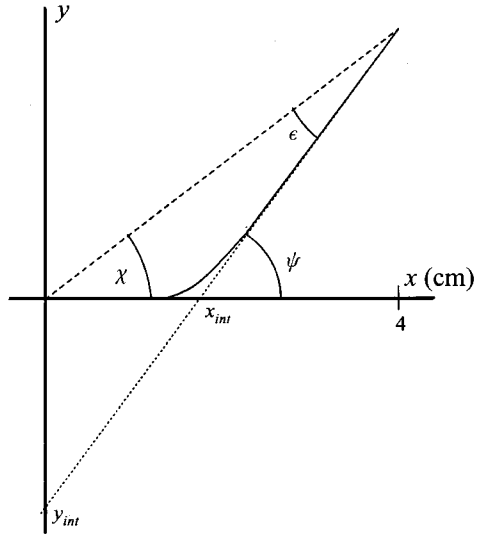

FIGURE 9. Trajectory angle χ computed for $x = 4$ cm and subject to parallax error angle ϵ; is the ψ , self-similar trajectory angle, free of parallax; x_{int}, y_{int} are coordinate intersections of the tangent to the self-similar part of the trajectory.

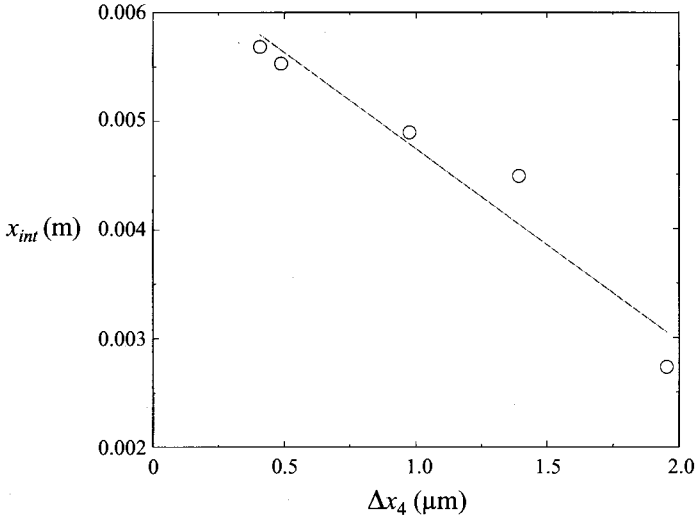

FIGURE 10. x_{int} versus Δx_4 at $\theta = 50.5°$. Linear fit to the calculated x_{int} is shown.

smooth flow, but only first-order in the presence of a discontinuous shock. Also shown is a linear fit to the computed x_{int},

$$x_{int} = 0.00652 - 0.00178\Delta x_4 \ . \tag{18}$$

The calculations reported in the remainder of this paper were performed with a resolution on the finest level $\Delta x_4 = 4.07 \times 10^{-7}$ m. Figure 10 clearly indicates that for $\Delta x_4 = 4.07 \times 10^{-7}$ m, the calculation is not fully converged. At this value of Δx_4 the calculated value of x_{int} is 0.00568 m while the linear extrapolation above suggests a converged calculation would measure 0.0065 m. Because of computational expense, we are not able to perform the calculations described below at a finer Δx_4. All

results should be implicitly understood to result from a calculation which is 85–90% resolved. However, some quantities, such as the asymptotic slope of the triple-point trajectory, are quite insensitive to the value of Δx_4.

4.6. *System diagnostics*

4.6.1. *Definition of the self-similar Mach number* $\hat{M}$

The numerical data were post-processed to obtain various quantities which could make it easier to understand the physics of the diffraction. Pressure p is a sensitive indicator of compression waves, while the contours of entropy s coincide with contact surfaces and with particle paths behind curved shocks, and they can also distinguish between shock and isentropic processes. The velocity component u is sensitive to the viscous boundary layer; and the temperature T, or equivalently the internal energy e, is sensitive to the thermal boundary layer; while v can reveal disturbances in the boundary layer.

One of the most useful diagnostic tools is the self-similar Mach number $\hat{M}$ which is defined in the following way. Let

$$\hat{x} = \frac{x - x_0}{t}; \qquad \hat{y} = \frac{y - y_0}{t}, \tag{19}$$

where (x_0, y_0) are the coordinates of a fixed reference point, such as the ramp corner. Now let,

$$\hat{u} = u - \hat{x}; \qquad \hat{v} = v - \hat{y}, \tag{20}$$

then

$$\hat{M} = (\hat{u}^2 + \hat{v}^2)^{1/2}/a \tag{21}$$

where a is the local speed of sound. When $(\hat{x}, \hat{y})$ are chosen to coincide with a wave node, then $\hat{M}$ is the flow Mach number in coordinates which are at rest with respect to the node. Note that in an ϵ-neighbourhood of the node $\hat{M} \to M$ (see for example the discussion in Jones, Martin & Thornhill 1951 or Sternberg 1959). Naturally $\hat{M}$ may be variable about the node. We often found it helpful to superimpose the $\hat{M} = 1$ contour on the graphics of other quantities such as p and s.

4.6.2. *Boundary layer diagnostics*

It has been noted (Mirels 1956; Mirels & Hamman 1962) that the negative displacement height of the boundary layer in the node-fixed coordinates induces a deflection in the particle path of angle ν at R, see figure 3(*c*). The deflection is caused both by the cooling of the isothermal wall which substantially increases the density $\rho(y)$ inside the boundary layer, especially at the ramp surface, and by the apparent *gain* in mass in node-fixed coordinates due to viscous action. One way to calculate ν is to calculate the boundary layer displacement height and then differentiate to obtain its slope at the node. But this requires the assumption that the displacement height is the appropriate one, and this may not be correct; it could be the momentum height for example. A better way, at least in principle, is to calculate ν from the change in $\hat{M}$ across the reflected shock r by using the ordinary shock wave equations for a perfect gas (AMES 1953). Thus for RR, the particle path deflection angles for the incident shock can be calculated from the given data γ, M_i, and θ, while δ_1 for the reflected shock can be calculated from the shock wave equations by extracting $\hat{M}_1$ and $\hat{M}_2$ from the numerical results. Here $\hat{M}$ is for coordinates at rest with respect to

the node R, so that $M_1 = \hat{M}_1$, $M_2 = \hat{M}_2$. In terms of δ_0, δ_1, the boundary condition for RR on the ramp for a viscous gas is

$$\delta_0 - \delta_1 + v = 0, \tag{22}$$

therefore

$$v = \delta_1 - \delta_0 < 0, \tag{23}$$

while for a non-viscous gas,

$$\delta_1 - \delta_0 = 0. \tag{24}$$

4.6.3. *Wave direction*

It will be useful to assign a direction to a wave by resolving the flow vectors relative to it, and upstream and downstream of it, into component vectors normal and parallel to the wave (von Neumann 1963; Glimm *et al.* 1985). Then the direction of any oblique wave is merely the same as that of the tangential vector component of velocity; this vector does not of course change across the wave. When an oblique wave points toward the node then it *arrives* there, but when it points away from it, then it *leaves* the node. Examples are shown in figures 1 and 2. An oblique wave will also be considered as being in either one of two families, in the same sense as $\pm$ characteristics. For example in figure 2(*a*), it i_1 and r_2 are, for example, in the first family, then i_2 and r_1 are in the second, while i_1 and i_2 arrive at the reflection node and r_1 and r_2 leave it.

5. Results and discussion

5.1. *Transition dynamics when $\theta < \theta_e$*

5.1.1. *Before the eruption of the Mach shock*

When $\theta < \theta_e$, experiments show that some form of Mach reflection (SMR, CMR, DMR) will appear, except perhaps when $\theta \to \theta_e$ from below which can lead to an indefinite result because of the difficulty of resolving the wave system. In our experiments with $\theta = 52°$ which is close to $\theta_e = 53.776°$, the shock system had the appearance of a regular reflection except that the i and r shocks apparently did not meet on the ramp surface. Instead there seemed to be a small gap g between them, see figure 11(*a*). Accordingly, it was described as an 'unresolved irregular reflection'. However, our numerical computations have a finer resolution than the schlieren apparatus and can resolve it. The wave system obtained numerically is sketched in figure 11(*b*) and the colour graphics for the velocity field u and pressure field p are presented in figures 12 and 13 respectively.

Figure 12 shows a time sequence of 15 images which cover a period of approximately 17.2 μs. Note the presence of the boundary layer on the ramp surface behind the initiating shock in each image. Each image shows a region 130×10^{-6} m square in the neighbourhood of the reflection point. The centre of the imaged region advances down the ramp with a speed of 1205 m s^{-1}. The speed of the incident shock was 742.1 m s^{-1} in the laboratory-frame coordinates. Figure 13 shows a time sequence of nine images starting at the same time as the first image of figure 12 and covering a interval of 19.2 μs. Images are separated by roughly 2.4 μs. In contrast to the images of figure 12, which show a region of constant spatial extent in the laboratory frame, the images of figure 13 show a constant extent in self-similar coordinates. Each image shows the same region, 1140 m s^{-1} $\leqslant \hat{x} \leqslant$ 1235 m s^{-1} and $0 \leqslant \hat{y} \leqslant 95$ m s^{-1}.

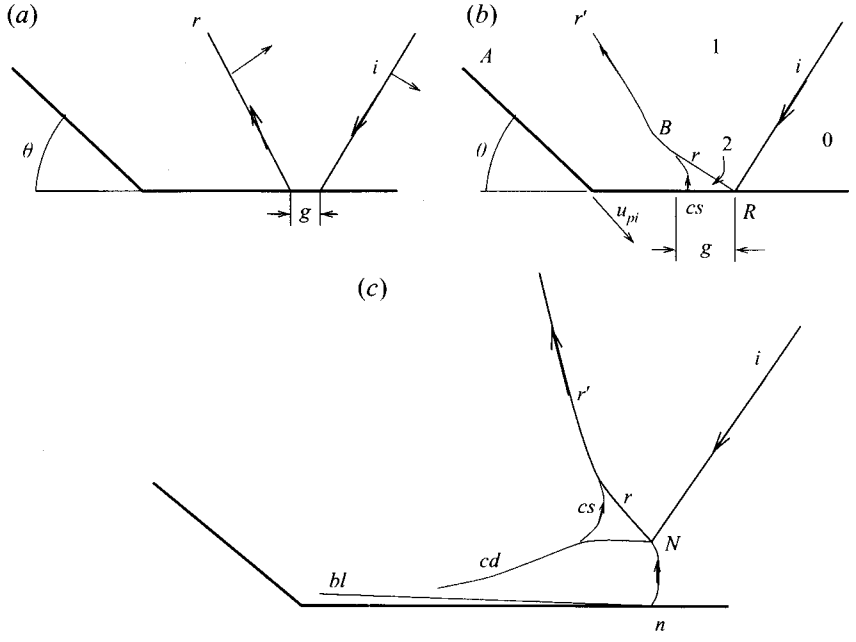

FIGURE 11. Experimentally observed and numerically resolved diffraction for $\theta = 52°$, $\gamma = 5/3$, $\hat{M}_i = 2.327$. (*a*) Unresolved irregular reflection observed in experiment; g is the 'gap'. (*b*) Computationally resolved diffraction; B, bend, interaction zone. (*c*) system after $cs \rightarrow R$ collision; n, Mach shock; N, shock triple-point node.

Figure 13 also has superimposed upon it the contour of the self-similar Mach number $\hat{M} = 1$.

The first seven frames of figure 12 have the same structure as shown in figure 11(*b*). The wave system consists of a pre-cursor regular reflection ($i - r$), but further downstream r is overtaken by the corner signal cs which forces r to bend smoothly at B into a steeper shock r' say. The $r - s - r'$ wave triplet has some similarity to what Colella & Henderson (1990) called a von Neumann reflection (VNR), except that cs arrives at the intersection zone B whereas in a VNR the corresponding disturbance leaves the zone. It is interesting to note that the pre-cursor regular reflection cannot exist for an ideal (inviscid, non-heat-conducting) gas when $\theta < \theta_e$. Is is only possible here because the existence of the boundary layer, as shown in figure 3(*c*), requires the use of equation (23) rather than (24).

5.1.2. *Eruption of the Mach shock*

It will be noticed from figure 12 that cs overtakes the reflection node somewhere around the ninth frame. So the pre-cursor system is dynamically unstable. After the $cs \rightarrow R$ collision, a Mach shock n and its associated shock-triple-point node N erupt from the ramp surface, see figures 11(*c*), 12, 13. The Mach shock travels with a greater velocity than the incident shock and consequently its length increases with time. The results show that n is faster than cs, so the distance between them now increases with time. With further development, which is not presented, the system evolves to the self-similar state called complex Mach reflection (CMR). In our $\theta = 52°$ experiment we photographed the shock system when it was about 4 cm along the ramp surface. According to the numerical results, a Mach reflection forms when the incident shock

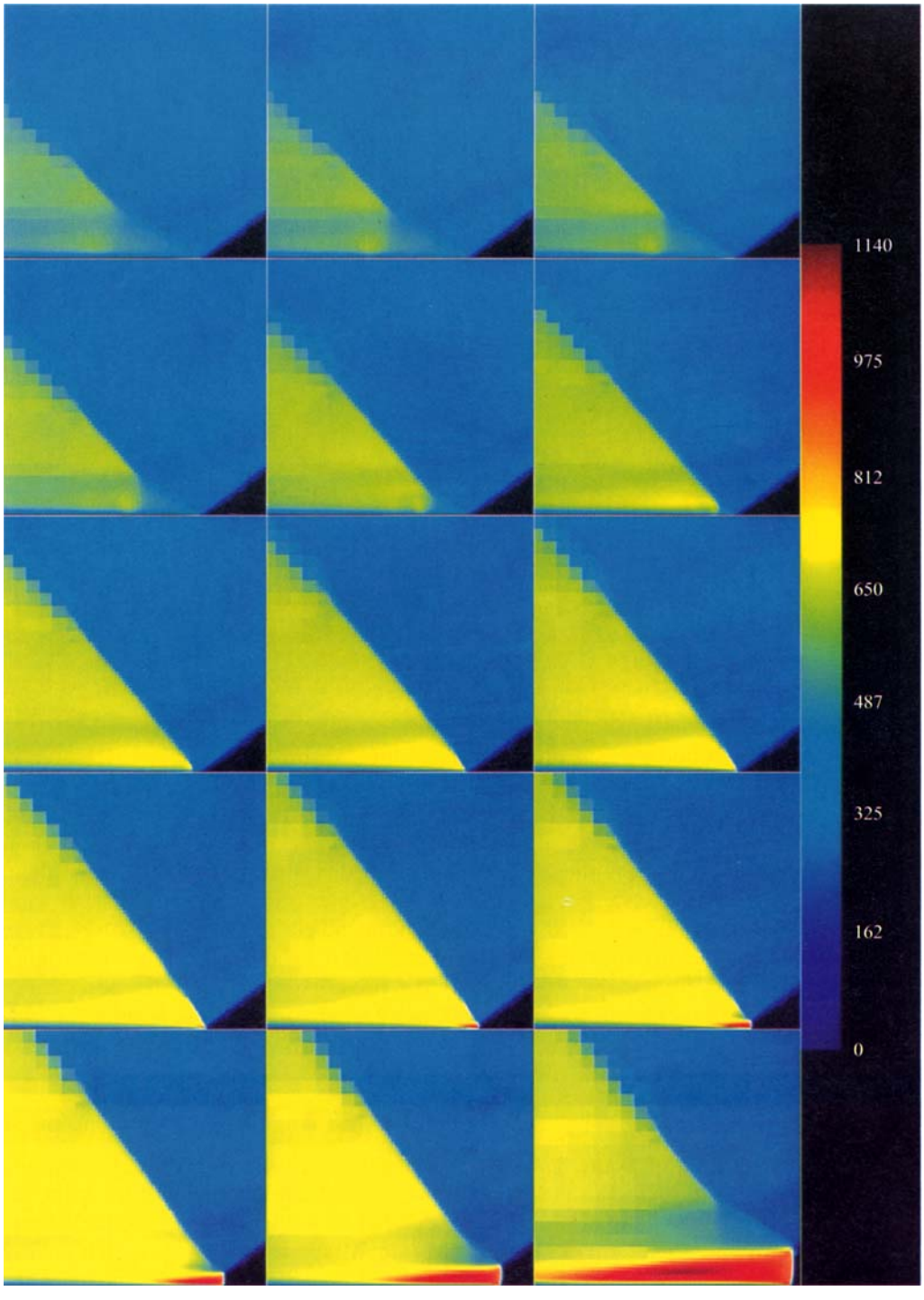

FIGURE 12. Time sequence of velocity component u, for $\gamma = 5/3$, $M_i = 2.327$, $\theta = 52°$; ramp surface shown horizontal. Sequence is left to right followed by top to bottom. Units are m s^{-1}.

FIGURE 13. Self-similar pressure and self-similar $\hat{M} = 1$ contour for $\gamma = 5/3$, $M_i = 2.327$, $\theta = 52°$. Units are Pa.

has travelled down the ramp for 1.5 cm, so the system we photographed must be a MR even though our schlieren apparatus could not resolve it. Our numerical calculations indicate that at 4 cm, the Mach stem should be 0.37 mm high, which cannot be resolved in our experimental apparatus.

The boundary layer and contact discontinuity *cd* are visible in the *u* field (figure 12), but not of course in the *p* field (figure 13). The Mach shock *n* is convex forward and actually arrives at the triple point *N* in figure 11. Strictly speaking, it is not a Mach node since *n* leaves such a node, see figure 1(*b*). Instead it is more like a cross-node as in figures 2(*a*) and 2(*b*), but one for which the flow Mach number which leaves say i_1 is subsonic. When this occurs r_1 cannot exist and the $(i_1 - i_2 - r_2)$ triplet comprises a 'degenerate' cross-node with i_1 and i_2 arriving and r_2 leaving the node. This implies that *n* in figure 11(*c*) is behaving like a pre-cursor which is being driven from its rear, presumably by the same disturbance that caused the $cs \rightarrow R$ collision. The discussion of this disturbance will be deferred to §5.1.4. Notice that *n* curves backwards as it approaches the ramp and that it is *not* perpendicular to the surface. This is a consequence of a mass sink that effectively exists at the foot of the shock and also due to the strong cooling at the isothermal wall which causes the gas density to increase by a factor of about 4 and the viscous displacement effect – the angle *v*. Seiler & Schmidt (1978) found somewhat similar effects especially for the shape of the Mach shock.

5.1.3. *The sonic surface*

Important results follow by superimposing the self-similar $\hat{M} = 1$ contour onto the self-similar p field, figure 13. The contour appears to coincide with the rear of the overtaking $cs - r'$ disturbance. A detailed study was done by extracting horizontal (y constant) and vertical (x constant) 'cuts' through the r' and cs disturbances. This showed that there was a positive entropy jump across r' and that the $\hat{M} = 1$ contour was embedded inside it. Furthermore, relative to r' the flow left it subsonically, so r' is a compression shock. By contrast it was found that cs was an isentropic compression and was terminated at its rear by the $\hat{M} = 1$ contour. This is further evidence that the overtaking disturbance $cs - r'$ is driven from its rear.

In summary, the $r - s - r'$ wave triplet comprises the r shock and the cs isentropic compression, both of which arrive at the interaction region B, and the r' shock which leaves it. The CMR thus appears to consist of a leading SMR followed by an $r - cs - r'$ wave triplet. A DMR would consist of a combination of two SMRs.

5.1.4. *The driving disturbance*

It will be convenient to continue with the $\theta = 52°$ example in considering what disturbance drives the overtaking $cs - r'$ wave composite. We abstracted the self-similar flow Mach numbers $\hat{M}_0$, $\hat{M}_1$, and $\hat{M}_2$ about the RR pre-cursor near R, then $\hat{M}_0 = 3.78$, $\hat{M}_1 = 1.96$, and $\hat{M}_2 = 1.18$. The maximum particle path deflection (detachment) angle across r for $\hat{M}_1 = 1.96$ is 18.8°. In the notation of Bleakney & Taub (1949) and Kawamura & Saito (1956), this corresponds to the wave angle for shock detachment $\omega_{ie} = 63.2°$. This angle is with respect to the oncoming particle path, but with respect to the ramp surface it is $\omega_{ie} = 42.1°$. However figure 12 shows that ω_1' increases to $\omega_1' \approx 50° > 42.1°$ as r bends smoothly at B to r', and this implies that r' is behaving like a shock detaching from a steep wedge. This is not surprising since $\theta = 52° < \theta_e$ implies that $\omega_0 > \omega_e$, where ω_0 is defined in figure 3, although in this case the trajectory virtually coincides with the ramp surface. In figure 11(b), the gas velocity along the surface A (upstream of the apex) is the driving piston velocity U_{pi} of the incident shock in laboratory-frame coordinates. The flow Mach number is $M_{pi} = 0.891 < 1$, so r' must detach from the ramp. Indeed the results show that r' everywhere moves away from the apex. It is concluded that it is the ramp itself, which with $\theta = 52°$ is a considerable blockage to the flow, is the disturbance which drives the $r' - cs$ composite wave as though it is a detaching shock. It overtakes the RR pre-cursor and forces the eruption of the Mach shock. Evidently r' will have a sonic point where cs arrives at B, and as r' continues to steepen through B it will also have a detachment point e'. With increasing steepness this detachment condition will be exceeded. Therefore as the $i - r$ pre-cursor is overtaken by the $r' - cs$ composite, then first the sonic point overtakes R causing the corner signal cs to vanish, then the detachment point overtakes, and the Mach shock erupts as the detachment point is passed. After eruption the corner signal reappears and the evolution to a self-similar CMR begins.

Remark

Dr Ralph Menikoff of the Los Alamos National Laboratory read an early version of this paper. He noted that, "Your section on the driving disturbance fails to explain *why* there is a delay in the corner signal overtaking the reflected wave". He offered us the following ingenious conjecture to explain this delay. His idea is based on an analogy with the Marshak thermal wave (Zeldovich & Raizer 1966). Suppose a block of metal is suddenly heated by thermal radiation. Then a thermal wave propagates

into the metal and the temperature increase behind the wave also raises the pressure. Usually a rapid rise in pressure will cause a shock. However in this case, the thermal wave initially moves faster than the shock, that is at supersonic speed. However the speed of the thermal wave falls off with distance and eventually becomes subsonic. The pressure disturbances can then organize into a shock which outruns the thermal wave.

Now consider the delay in the overtaking of the corner signal. The diffusion of momentum and heat in the boundary layer is analogous to the conduction of heat in the metal. The boundary layer propagates into the compressed argon downstream of the pre-cursor RR node (figure 11*b*). The temperature changes inside the boundary layer also cause dynamic pressure disturbances. If the boundary layer thickness is say y^*, then it propagates at a definite velocity, say v^*, in the y-direction. Since the boundary layer is exceedingly thin near the node it will be assumed to be laminar, so by the Blasius theory, $y^* \propto x/(Re)^{1/2}$, where $Re = ux/\eta'$ is the Reynold's number, x is the distance from the pre-cursor RR node, u is the gas velocity just outside the boundary layer in the x-direction, and η' is the kinematic viscosity $\eta' \equiv \mu/\rho$. Therefore $y^* \propto (x\eta' t/x)^{1/2} \propto (\eta' t)^{1/2}$, where t is the time. Then $v^* = dy^*/dt \propto (\eta'/t)^{1/2}$. Now when the node is near the ramp apex, then t will be small for any particular x. In this case v^* may exceed the speed of sound of the compressed argon $v^* > a_2$, that is the boundary layer (analogous to the Marshak wave) propagates at supersonic speed in the y-direction. But with increasing time, v^* decreases as $1/t^{-1/2}$, and in a time of the order of $t \geqslant \eta'/a_2^2$ the diffusing boundary layer wave thereafter moves at subsonic speed. But this now means that more flow enters the boundary layer than it can accommodate. The pressure disturbances now propagate out of the boundary layer to both retard the incoming flow and to form the corner signal. As we have seen, the corner signal is not a shock in this case but an isentropic compression.

5.1.5. *Experiments of the Lock–Dewey type*

During their experiments with weak shocks (ours are strong) Lock & Dewey (1989) generated sonic signals downstream of the shock system. They found that the signals overtook the regular reflection at, or near, transition, but that this condition was *not* the same as the sonic point criterion obtained from the ideal von Neumann theory. A similar effect exists with our results, for if such experiments were done with our strong shocks with the $\theta = 52°$ ramp but *before* the eruption of the Mach shock, then there is a sonic surface at the rear of the corner signal. The eruption of the Mach shock is very close to the point where the sonic surface overtakes the pre-cursor RR (in the 8th frame of figure 12). Yet $\theta = 52°$ is *not* the same as the sonic point angle $\theta_s = 53.294°$ (table 1) obtained from the inviscid theory.

5.1.6. *The boundary layer disturbances*

An example of the disturbances in the v, u, p, and e fields is presented in figure 14. Notice the large-amplitude disturbances in the boundary layer revealed by the v field. They are associated with the corner signal *cs* which is visible in the p field. As *cs* sweeps over the boundary layer, it is associated with a downwelling of gas on its leading edge and an upwelling just behind the corner signal. On the upstream side of the corner signal $v \approx 70$ m s^{-1} downwards and on the downstream side it is about $v \approx 7$ m s^{-1} upwards. The shear in v is however small compared to the shear in u. The boundary layer is strongly thinned underneath it and rapidly thickened behind it, which must cause order of magnitude changes in the gradient of T.

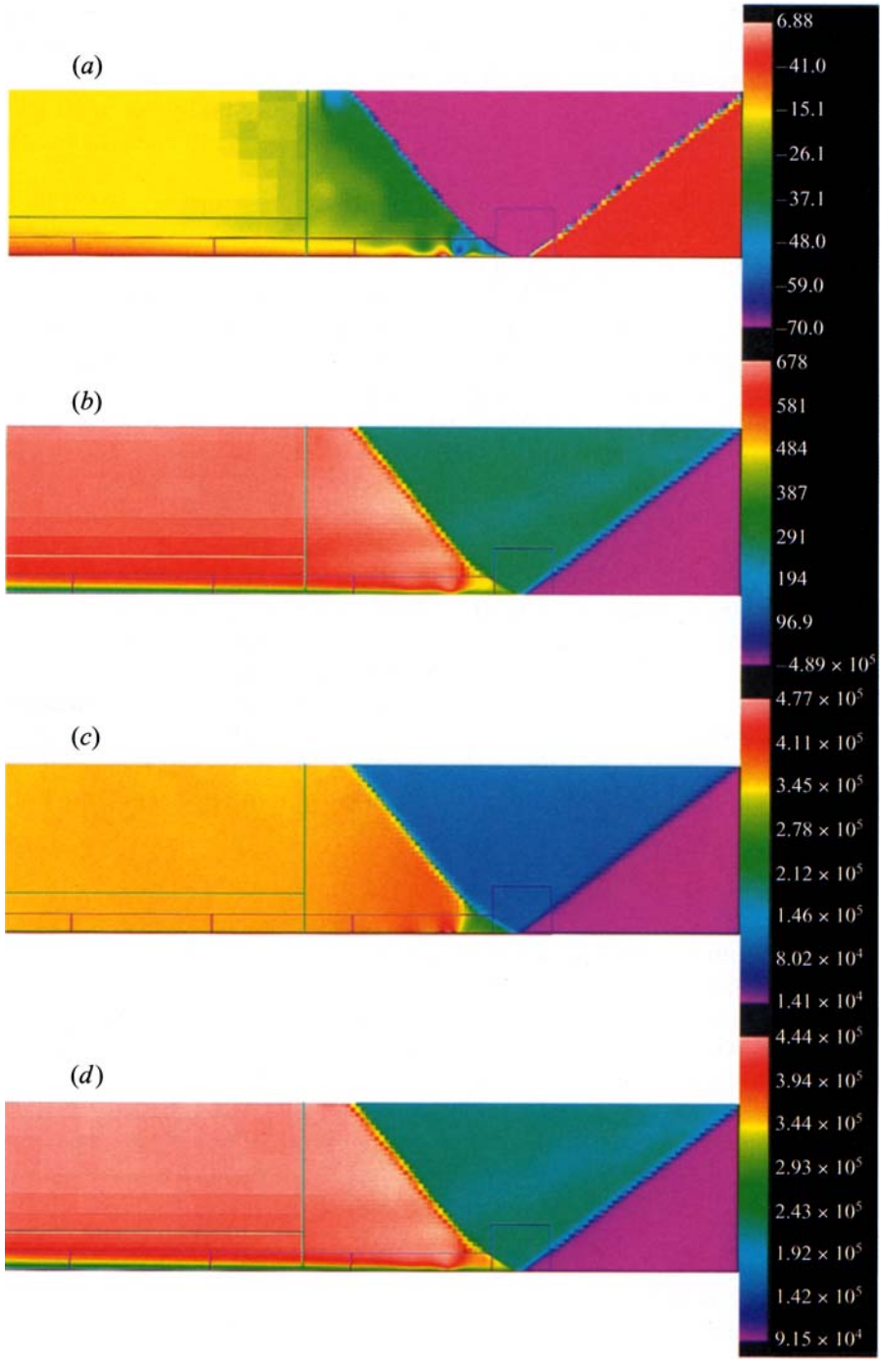

FIGURE 14. Flow near pre-cursor regular reflection for $\gamma = 5/3$, $M_i = 2.327$, $\theta = 52°$. Each display is 247×10^{-6} m long and 57×10^{-6} m high. At this time the shock has traversed 0.0128 m of the computational domain. The quantities shown are (*a*) v in m s^{-1}; (*b*) u in m s^{-1}; (*c*) pressure, in Pa; (*d*) internal energy, in (m s^{-1})^2.

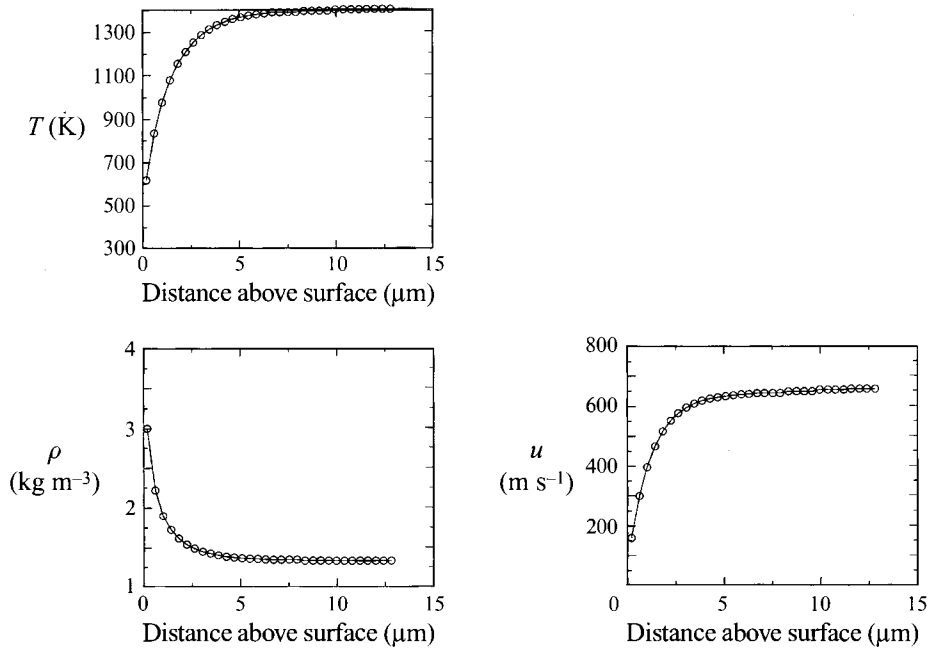

FIGURE 15. Boundary layer profiles at $\theta = 52°$. Location of profiles is 41×10^{-6} m behind the shock in the preceding figure.

The initial temperature of the gas is $T_0 = 293.15$ K and this is also the temperature of the isothermal surface of the ramp. Here the maximum temperature of the compressed gas is about 1400 K. The gas in the boundary layer is thus strongly cooled near the surface, in fact its density increases by a factor of more than 4. Some profiles are presented in figure 15. Our results show that the pressure change across the boundary layer is small so we display no graph for pressure.

For $\theta = 52°$, we had for the RR pre-cursor that $\hat{M}_0 = 3.78$, $\hat{M}_1 = 1.96$, $\hat{M}_2 = 1.18$. From these data it is calculated that the effective slope of the boundary layer at the pre-cursor node R is $v = -4.66°$. The boundary layer actually makes the pre-cursor possible by virtue of equation (23), but when the ideal gas boundary condition (24) applies, then an RR is impossible according to the theory of von Neumann.

5.2. *Numerical results for an ideal gas*

The diffractions that we have discussed above have also been studied numerically by Professor P. Colella, but he used the Euler equations instead of the Navier–Stokes equations. He treated the argon as though it were an ideal, inviscid, and non-heat-conducting gas. As a consequence of the ideal gas assumption, the following boundary conditions are satisfied at the ramp surface:

$$\frac{\partial u}{\partial y} = 0 = \frac{\partial T}{\partial y}. \tag{25}$$

Some of these results are presented in figure 16 for the trajectory angle χ of the shock triple point N (figure 1*b*) versus θ. Some experimental data are shown for comparison. A quadratic curve of best fit through the Euler calculations is

$$\chi = 26.4137 - 0.636977\theta + 0.00301802\theta^2. \tag{26}$$

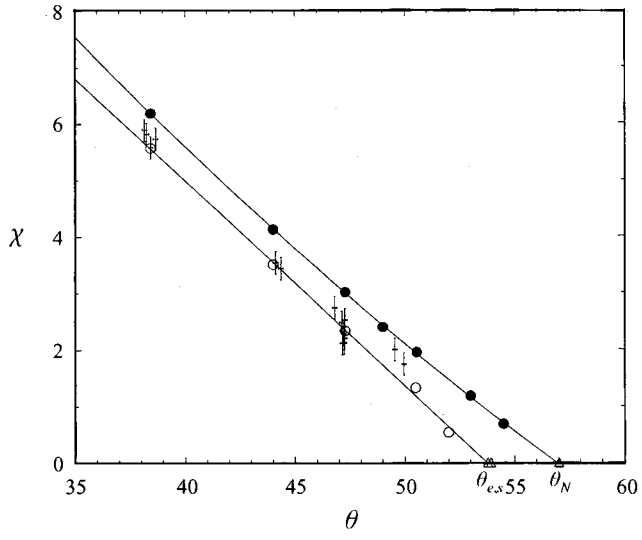

FIGURE 16. Trajectory angle χ of the shock triple point versus ramp angle θ for $\gamma = 5/3$, $M_i = 2.327$. Data from experiment, Euler calculations, and Navier–Stokes calculations are shown. Experimental data shows measurement error bars. A quadratic fit to the Euler calculations is shown as well as a linear fit to the Navier–Stokes results. The three transition criteria are indicated on the graph.

When this equation is solved to find the intercept with $\chi = 0$, one gets 56.699° which is close to the von Neumann point at $\theta_N = 57.021°$. There is a clear systematic discrepancy between the numerical Euler predictions and experimental results shown in figure 16 such that the Mach shock grows a little more slowly (smaller χ) for the real gas of the experiments than it does for the ideal gas of the Euler numerical computation.

In the numerical simulations of the Euler equations it is found that the triple-point trajectories are negligibly different from a straight line. The Mach shock thus grows uniformly with time; it is self-similar. More generally the results show that the flow is everywhere closely self-similar and that the diffraction pattern is a CMR. These results also mean that the parallax assumption is obeyed. Another consequence of the ideal gas assumption is that (24) is satisfied at the ramp surface.

5.3. *Numerical results from the Navier–Stokes calculations with isothermal and non-slip boundary conditions*

The numerical simulation of the Navier–Stokes equations takes into account the real gas properties of shear viscosity and thermal conductivity. The boundary conditions on the ramp surface are isothermal and non-slip,

$$u = 0, \qquad T = T_0 = 293.15 \text{ K}. \tag{27}$$

These boundary conditions force the existence of a boundary layer on the ramp surface.

When measuring χ from experimental data, the parallax assumption is sometimes made implicitly, in fact it is practically unavoidable if only one photograph is taken for each experiment. This was the case for the experimental data shown in figure 16. The photographs were taken after the incident shock i had travelled about 4 cm along the ramp, and χ was measured from the photograph by using the parallax assumption.

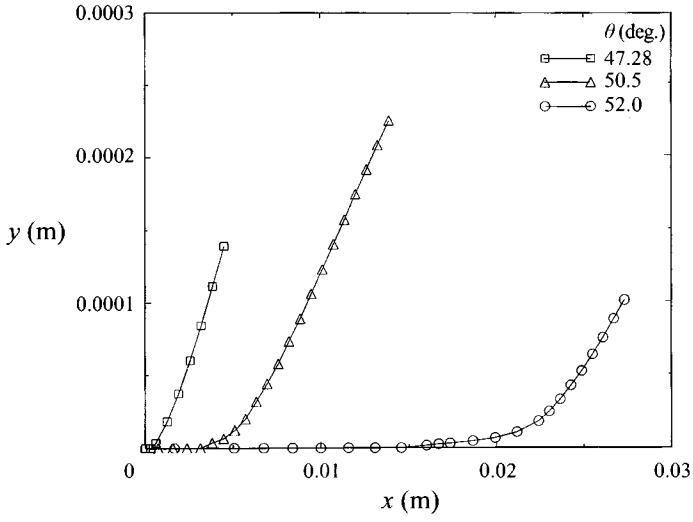

FIGURE 17. Numerical triple-point trajectories for viscous, heat-conducting argon, $\gamma = 5/3$, $M_i = 2.327$, at several wedge angles θ.

In the numerical simulations of the Navier–Stokes equations, this same measurement process was repeated in order to make a correct comparison of simulation with experiment. From each simulation, the (x, y) coordinates of the shock triple point N were extracted as the incident shock travelled up the ramp. Generically the trajectories had the form of a curve which asymptotes to a straight line at large x. The asymptote corresponds to the self-similar later portion of the triple point's trajectory. Figure 17 shows triple-point trajectories for several ramp angles measured from the Navier–Stokes simulations. Ideally one would extract from the simulation trajectory the y position of N at $x = 4$ cm. However, in order to minimize computational effort, most simulations were terminated before the incident shock had travelled more than 2.5 cm. The asymptoting line was then used to extrapolate the y position of the triple point to $x = 4$ cm along the ramp. Care was taken to run each simulation long enough to accurately determine the asymptoting line. Figure 9 demonstrates the extrapolation. The results of measurement of χ are presented in figure 16 and the quadratic curve of best fit through these data is

$$\chi = 19.44145 - 0.359069\theta - 5.18962\ 10^{-5}\theta^2. \tag{28}$$

The quadratic fit intersects $\chi = 0$ at $\theta = 53.727°$, which is close to the *detachment point* at $\theta_e = 53.776$.

Figure 9 also demonstrates the differences between the three angles which characterize the trajectories: χ is the experimentally observable angle that is plotted in figure 16; ψ is the angle of the self-similar portion of the triple-point trajectory; ϵ is the parallax displacement error.

Thus subject to the parallax assumption the effect of the viscosity and thermal conductivity upon the computations is to reduce χ for a given θ, as compared to the ideal (Euler) gas numerical calculation. The real gas properties slow the rate at which the length of the Mach shock increases, and also apparently shift the transition criterion from the von Neumann point to the detachment point. Additionally, the agreement with the experimental data has been improved.

5.4. *Numerical test of the parallax assumption*

It is of interest to examine the parallax assumption in more detail. The (x, y) coordinates of the triple point N were extracted from the Navier–Stokes numerical simulations at each time step to find out if the trajectory of N was in fact a straight line through the apex. Some results are presented in figure 17 and it is clear that every trajectory is curved. For example, it has been mentioned that for $\theta = 52°$ the Mach shock erupts not at the apex but at about 1.5 cm down the ramp, corresponding to the ninth frame of figure 12. After eruption the trajectory is curved for a time, but soon becomes a straight line, although not of course through the apex. Once the trajectory becomes straight the Mach shock length grows uniformly in time, that is, it becomes self-similar and indeed the whole system becomes self-similar. All of the trajectories have the same kind of behaviour. This phenomenon has been reported in experiments with shocks in low-density gases (Seiler & Schmidt 1978; Walenta 1987). It is concluded that the parallax assumption that the trajectory of the shock triple point is a straight line through the apex of the ramp is incorrect for a viscous, heat-conducting gas with isothermal and non-slip boundary conditions.

5.5. *The self-similar trajectory angle* ψ

There is of course nothing special about $x = 4$ cm. It was merely the approximate position of the shock system on the ramp when the photographs were taken in the experiments. But because the trajectories are curved, the values of χ will not be independent of this length scale, see figure 9. A trajectory angle ψ which *is* independent of the observation position x can be defined by the slope of the straight portion of the trajectory; it will be called the self-similar trajectory angle. The scale-free ψ extracted from the Navier–Stokes calculations is presented in figure 18. The quadratic curve of best fit through the data is

$$\psi = 25.1069 - 0.647699\theta + 0.0035933 8\theta^2. \tag{29}$$

The intersection of the quadratic fit with the line $\psi = 0$ is $\theta = 56.429°$ which is clearly closest to the von Neumann point $\theta_N = 57.021°$. It was impractical to extend the calculations into the decisive range $\theta_e < \theta < \theta_N$ because of computational cost. The computation for $\theta = 52°$ which came closest to this critical range required 30 hours of CPU time on a Cray-YMP. Nevertheless the results do support the conclusion that the von Neumann point is the criterion for regular $\rightleftharpoons$ irregular transition for self-similar strong shock diffraction over a rigid ramp with isothermal, non-slip boundary conditions.

As shown in figure 9, it is possible to define an angle of parallax error ϵ,

$$\epsilon \equiv \psi - \chi. \tag{30}$$

At later times when the trajectory has become straight and the system self-similar, the parallax error ϵ tends to zero, so $\chi \to \psi$. In fact, according to (28) and (29), the parallax error is less than 1% when $\theta \leqslant 43.4°$. To understand this, one can calculate the intercept x_{int} that the self-similar trajectory makes with the ramp when its tangent is extrapolated to $y = 0$. Similarly y_{int} can be defined from figure 9 as

$$y_{int} = -x_{int} \tan \psi. \tag{31}$$

Table 3 shows the analysis of Navier–Stokes calculations at six angles.

The viscous/thermal properties of the gas introduce the length scale x_{int} into each flow, but for fixed θ the effect becomes negligible at later times or larger distances

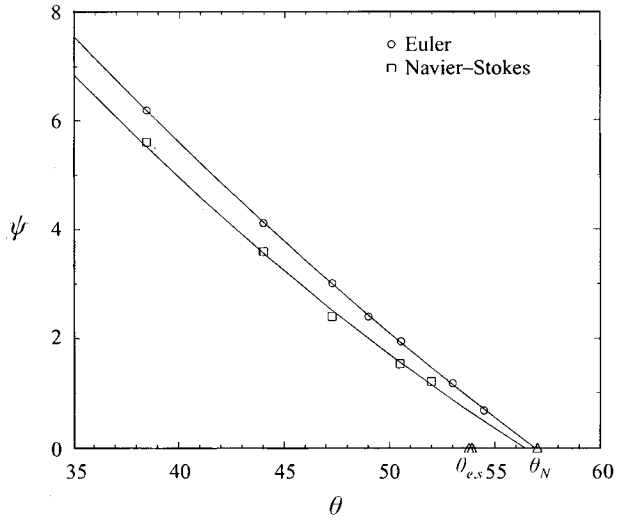

FIGURE 18. Self-similar trajectory angle ψ of the shock triple point. For the Euler calculations where the diffraction is self-similar, ψ is the same as χ. For the Navier–Stokes calculations, ψ differs from χ particularly as the transition is approached. The three transition criteria are indicated on the graph.

θ	34.6	38.6	44.0	47.28	50.5	52.0
ψ (deg.)	6.990	5.603	3.593	2.405	1.535	1.209
x_{int} (μm)	81.8	220	560	1200	5500	22500
y_{int} (μm)	−10	−21.6	−35	−50	−150	−447

TABLE 3. x_{int} and y_{int} of the self-similar trajectories with the ramp

when $x \gg x_{int}$. By comparing the numerical and experimental results only the two experimental data points for $49° < \theta < 50°$ are affected by the parallax error. Consequently for these two experimental data points $x = 4$ cm was too small a distance at which to take the photograph. For this angle of θ we needed to do the experiment at about 8 to 10 cm. However, the parallax error is negligible for the rest of the experimental data.

5.6. *Dependence of x_{int} upon θ*

We have previously stated that the Navier–Stokes calculations support the conclusion that the von Neumann point is the criterion for regular $\rightleftharpoons$ irregular transition for self-similar strong shock diffraction, i.e. that $\psi \to 0$ as $\theta \to \theta_N$, see figure 18. We have also stated that measurements of χ are not always good estimates of the self-similar trajectory angle because of the failure of the parallax assumption. Indeed, in general χ will depend upon the distance along the ramp where it is measured. However, it is evident that the χ angles obtained from the Navier–Stokes calculations, see figure 16, appear to go to zero as θ approaches the other criteria angles, θ_s and θ_e. We now consider this effect.

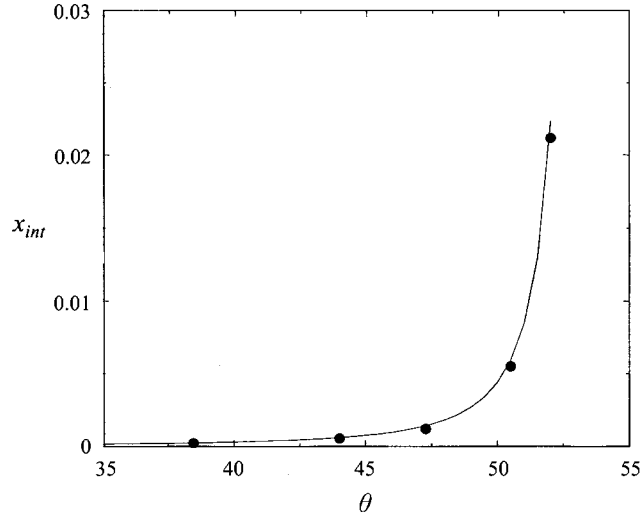

FIGURE 19. X intercept x_{int} versus ramp angle θ for $\gamma = 5/3$, $M_i = 2.327$. Also shown is fit to data of form $0.057243/(53.6 - \theta)^2$.

In figure 19 we have plotted x_{int} as defined in figure 9, as a function of θ. The measured x_{int} give every indication of becoming singular at a finite value of θ. Figure 19 shows that a very good fit to the available data is

$$x_{int} \approx \frac{0.057243}{(53.6 - \theta)^2}. \tag{32}$$

The choice of 53.6° as the singular angle is not meant to exclude other angles, in particular θ_s or θ_e. For the simple functional form of (32), 53.6° gives the best fit, but other functional forms cannot be excluded given the available data.

Let us assume that x_{int} does in fact become singular for θ in the neighbourhood of 53.6°. Consider any fixed distance d (4 cm say) along the ramp, and suppose that the ramp angles θ are such that $x_{int}(\theta) < d$, and also such that the trajectory becomes self-similar before reaching distance d on the ramp, as in figure 9. Then one has the relation

$$\chi = \arctan\left(\tan\psi\left(1 - \frac{x_{int}}{d}\right)\right). \tag{33}$$

When $x_{int} \ll d$, $\chi \approx \psi$. But as x_{int} increases and becomes comparable to but still less than distance d, (33) shows that $\chi < \psi$. Finally as x_{int} approaches distance d, then the y coordinate of the trajectory at d will become smaller and approach zero. Therefore, χ will be driven to zero even while ψ remains finite. This is possible because ψ is independent of d while in general χ depends on d. By our assumption that x_{int} diverges near 53.6°, we are led to the conclusion that χ is driven to zero at the same angle.

The intercept x_{int} is similar in scale to the distance the shock travels along the ramp before the Mach shock erupts. We have already described the eruption of the Mach shock as occurring when the corner signal cs overtakes the reflection node. If we further assume, as seems unavoidable, that the distance of overtaking also is singular near 53.6°, this suggests that the speed of the corner signal becomes equal to the speed of the reflection node at that angle.

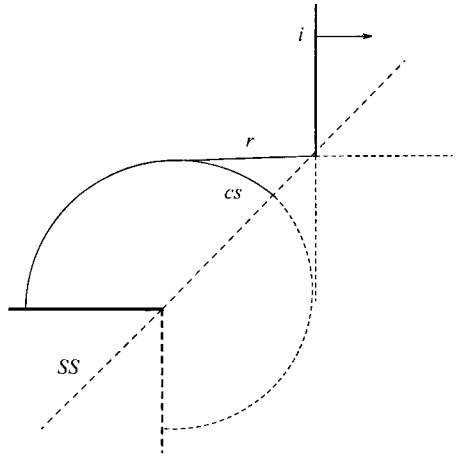

FIGURE 20. Conception of a self-similar, symmetric reflection without a boundary layer.

5.7. *The effects of the boundary layer on the rate of growth of the Mach shock*

It is also possible to obtain self-similar strong shock diffraction by using internal cavities as in figure 2(*b*). Experiments with these devices have been done by Smith (1959), Henderson & Lozzi (1975), and Virgona (1993). It is clear that for *symmetric* cavities the temperature and the velocity vector are the same for any two points $(x, \pm y)$ that are reflected in the plane of symmetry SS. So SS is a perfect adiabatic boundary with no viscous shear along it, thus no boundary layer. Therefore the boundary conditions (25) apply along SS. Additionally SS behaves as though it is an infinitely rigid wall. Thus even for a real gas, the plane of symmetry is a perfect adiabatic, slipping, infinitely rigid surface with boundary conditions (25), and which can be closely realized physically.

The boundary conditions can now be applied to the ramp by imagining a mirror image of the diffracting system in which the ramp surface is now the plane of symmetry SS, as in figure 20. This procedure simulates the self-similar cavity diffraction. If the previous ramp Navier–Stokes calculations are now repeated using the new boundary conditions (25) instead of the physical ramp boundary conditions (27), then the net effect will be to remove the viscous, heat-conducting boundary layer even though we are retaining the finite viscosity and thermal conductivity of the argon. The results for triple-shock-point trajectories θ less than or approximately equal to θ_e are presented in figure 21. When $\theta \ll \theta_e$, the trajectories are straight lines which pass through the apex with great precision: for example for $x = 0$ the discrepancy in y is about 3.3 μm when $\theta = 50.5°$. It follows at once that such systems are immediately irregular when $\theta < \theta_e$ and self-similar CMRs. There is then no parallax error ϵ and $\chi = \psi$. Since the boundary layer has been removed these conditions imply that (24) applies locally on the ramp instead of (23).

As the ramp angle θ approaches θ_e, the trajectories become distorted from straight lines. This will be discussed in the next subsection.

When we plotted these ψ versus θ Navier–Stokes calculations we obtained the extraordinary result that they were in close agreement with the results from the ideal gas Euler calculations, see figure 22. There is actually a small systematic displacement of approximately 0.1° from the Euler results such as to reduce the rate of growth of the Mach shock slightly.

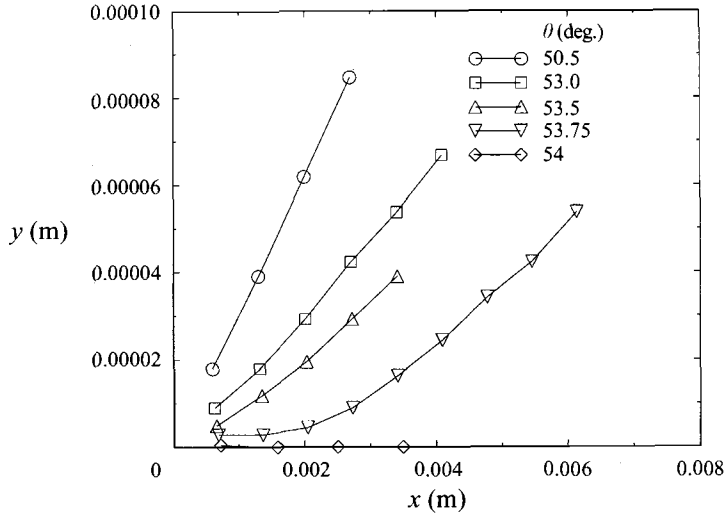

FIGURE 21. Numerical trajectories of the shock triple point in a viscous, heat-conducting gas with adiabatic/slip boundary conditions on the ramp surface. θ is in the neighbourhood of $\theta_e = 53.776°$. Note in particular $\theta = 54°$.

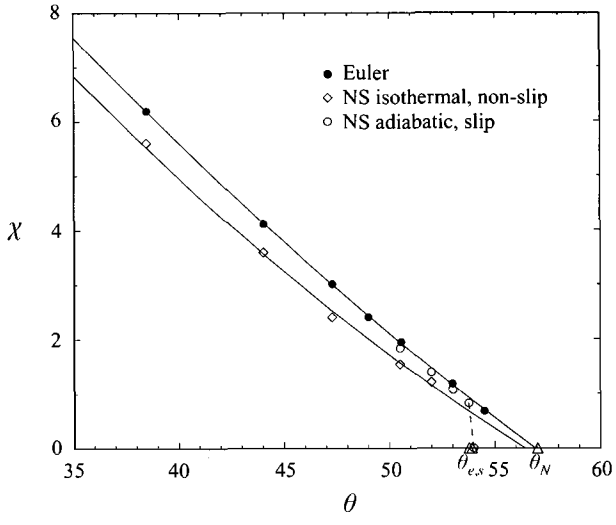

FIGURE 22. Self-similar trajectory angle ψ for Euler equation and Navier–Stokes equations with two different boundary conditions on the ramp. Lines indicate best quadratic fit to the Euler data and to the Navier–Stokes with isothermal and non-slip boundary conditions. The three transition criteria are indicated on the graph. Dashed line shows abrupt transition of Navier–Stokes with isothermal and non-slip boundary conditions near 54°.

On comparing the results of the Navier–Stokes simulations for boundary conditions (25) and (27) it is concluded that the viscous, heat-conducting boundary layer is the dominant influence in reducing the self-similar rate of growth of the Mach shock. This fact has long been suspected by some researchers. The small discrepancy between the Euler and the Navier–Stokes adiabatic/slip results is attributed to momentum and heat transfer in the diffusing contact discontinuity, although this is an open question.

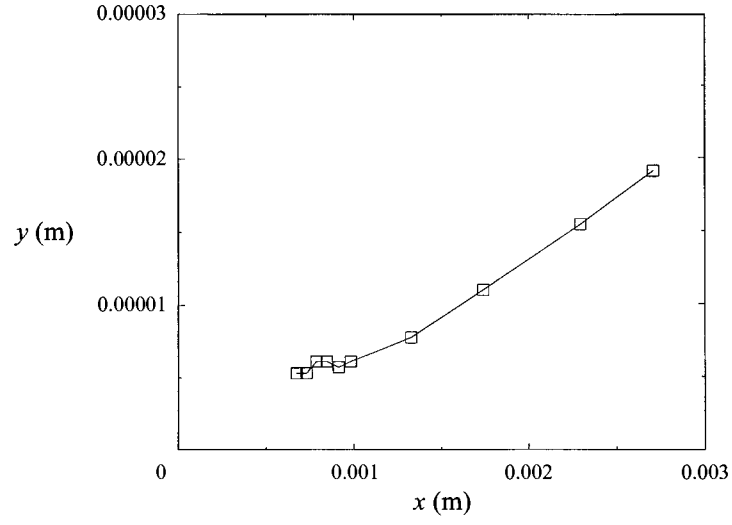

FIGURE 23. Triple-point trajectory for Navier–Stokes equation with adiabatic and slip boundary conditions on ramp surface; $\theta = 54°$. Navier–Stokes calculation was initialized with data from an inviscid calculation which had Mach stem 5 μm high.

5.8. *The range* $\theta_e \leqslant \theta \leqslant \theta_N$

In this range (24) can be satisfied for an ideal gas, while a real gas satisfies (23). In either case, a regular reflection is now possible. The Euler calculations in this range still support the von Neumann point, see figures 16, 18, and 22. Although the Navier–Stokes calculations with the isothermal/non-slip boundary conditions (27) also support this point once self-similarity is established, the prohibitive cost of the calculations made it impracticable to extend the ψ versus θ curve into the range.

However for the adiabatic/slip boundary conditions (25) it is possible to economically perform the computations in this angular range, and for this range the calculations produced a regular reflection. The ψ versus θ curve was explored numerically near the θ_e point. In particular ψ was calculated for $\theta = \theta_e \pm 0.1°$, and it was concluded that the Navier–Stokes calculation indicated a discontinuity in the ψ at θ_e. Figure 22 shows the discontinuity in trajectories for θ near $\theta_e = 53.776$. As θ approaches θ_e from below, the triple-point trajectories increasingly deviate from straight lines. Because of the adiabatic, slip boundary conditions, there is no physical boundary layer in these calculations. Examinations of the velocity and temperature fields from the Navier–Stokes calculations do not show any evidence of a numerical boundary layer.

As discussed above, Euler calculations in this range of θ *do* form a Mach shock, while the Navier–Stokes calculations do not. It is interesting to ask whether the Navier–Stokes calculation can support a Mach shock if it already exists. This is accomplished numerically by running an Euler calculation for a few steps until it has formed a Mach stem 5 μm high. The data from the Euler calculation are then used to initialize the Navier-Stokes calculation, see figure 23. Clearly the Navier–Stokes calculation can support a Mach shock once it has formed.

The numerical results and experiments suggest the intriguing possibility that in the range $\theta_e \leqslant \theta \leqslant \theta_N$ with slip, adiabatic boundary conditions, there are two stable configurations, corresponding to regular reflection and Mach reflection. The regular reflection configuration is only slightly stable and is not observed experimentally

because slight perturbations either from imperfections in the experimental apparatus or statistical fluctuations in the gas move the state out of the region of stability. The Navier–Stokes calculations have neither imperfections in the surface of the ramp nor fluctuations in the gases, and thus can produce a regular reflection. However, if the Navier–Stokes calculation is initialized with a configuration closer to the Mach reflection than the regular reflection, it quickly relaxes into the Mach reflection form.

This hypothesis would further suggest that the regular reflection configuration is less stable for the Euler equation than for the Navier–Stokes equations because the Euler calculations always produce Mach shocks in this angular range. In this case, the perturbations which destroy the RR configuration would arise from the numerics. In contrast, the Navier–Stokes calculation is stabilized by the presence of momentum and heat diffusion. Numerical perturbations, if they are sufficiently small, can be diffused away in the Navier–Stokes simulation before they can cause a major deviation in the solution.

If experimental or statistical fluctuations are responsible for the observation of the Mach stem in cavity experiments in the range $\theta_e < \theta < \theta_N$, this opens the possibility that such fluctuations may also affect the eruption of the Mach stem in experiments when $\theta < \theta_e$, even for ramp experiments. This is an open question deserving serious study.

5.9. *Heat transfer versus viscosity effects*

In order to obtain an estimate of the relative magnitude of these effects on the eruption of the Mach shock, the $\theta = 52°$ calculations were repeated with different boundary conditions. In the first of them, the ramp was made adiabatic and non-slip,

$$u = 0 = \frac{\partial T}{\partial y}, \tag{34}$$

and then conversely,

$$\frac{\partial u}{\partial y} = 0, \qquad T = 293.15 \text{ K}, \tag{35}$$

that is a slip boundary with an isothermal surface. The results are presented in figure 24 as curves C and D respectively. The eruption begins at about 0.65 cm for curve D and at about 0.21 cm for curve C. So in this case the heat transfer delays the eruption about three times as much as the viscosity does.

5.10. *On the criterion for RR → CMR transition in a real gas*

An extraordinary result is that a tangent to the real gas curve ψ versus θ for angles $\theta < 45°$ will, if extended to $\psi = 0$ pass through or very close to the ideal gas θ_e point, see figure 18. This is further support for the conclusion that a CMR comprises an SMR followed by a wave composite $r' - cs$ which acts like a detaching shock. For the self-similar conditions of ψ versus θ, the parallax error is of course zero. The parallax error for χ is negligible when $\theta < 45°$, because then $x \gg x_{int}$, when $x \approx 4$ cm. Thus the blockage to the flow due to the ramp is the dominant effect when $\theta < 45°$, the real gas only causes the Mach shock to grow somewhat more slowly than in an ideal gas.

In order to explore the matter further, some data for the angle η that the contact discontinuity cd makes with the ramp are presented in table 4. From figure 25,

$$\eta = \psi + \delta_n \tag{36}$$

and δ_n is the particle path deflection through the Mach shock at the triple point. In

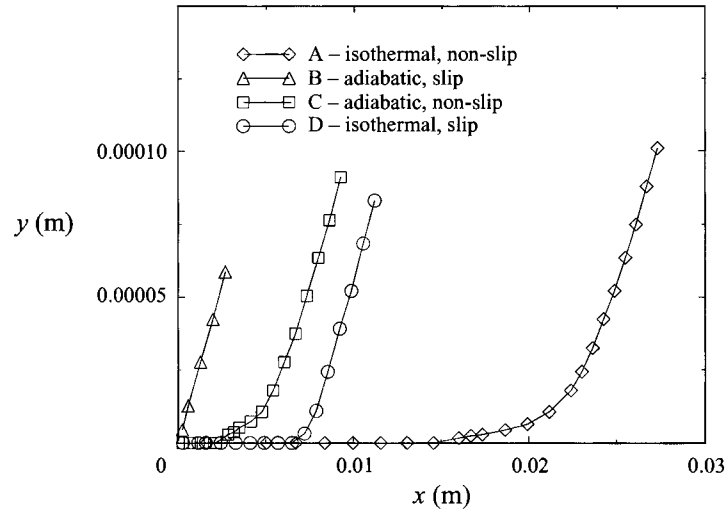

FIGURE 24. Effects of various boundary conditions on the trajectory of the shock triple point when $\theta = 52°$. (x, y) are the shock triple point coordinates.

θ	34.6	38.6	44	47.28	50.5	52	53.776	57.021
δ_n	16.4	13.7	9.83	7.59	5.11	3.89	2.61	0
η	23.4	19.3	13.4	10.0	6.65	5.10	3.28	0

TABLE 4. Impact angle η of the contact discontinuity on the ramp surface

order to calculate a particular δ_n, the angle ω_0 from figure 3(*a*) was extracted from the Navier–Stokes data, and used as input to the inviscid von Neumann theory to find δ_n. At $\theta = 34.6°$ the contact discontinuity *cd* and its nearby particle paths impact on the ramp at the comparatively steep angle of $\eta = 23.4°$, but this becomes steadily smaller as $\theta \to \theta_e$. If the curve were extended to θ_N, then $\eta = 0 = \psi = \delta_n$, and the *cd* would not only then be parallel to the ramp, but would coincide with its surface. This means that the local flow about the shock triple point is increasingly influenced by the surface boundary conditions as θ gets smaller, and consequently less influenced by the ramp blockage.

Now the detachment condition is only available for $\theta \leqslant \theta_e$, so *if* a CMR is to exist in the range $\theta_e \leqslant \theta \leqslant \theta_N$, then some other dynamical process must induce the transition RR $\rightleftharpoons$ CMR. It is noted that since the theory allows either of these systems to occur, then the one that actually occurs will have its stability under constant test by the fluctuations which are invariably present for a real gas flow. Now the two-state flow along the *cd* in a Mach reflection has both a temperature and a velocity discontinuity across the *cd*, so the two-state flow is not even in thermal or dynamic equilibrium, let alone stable. However the shock system is stable even though the two-state flow downstream is not. Otherwise a Mach reflection could not exist and this would contradict experiment. It seems plausible therefore that if an RR appears in the range, then the fluctuations could cause transition to the CMR by 'discovering' the thermodynamically and dynamically unstable two-state flow, but this is also an open question.

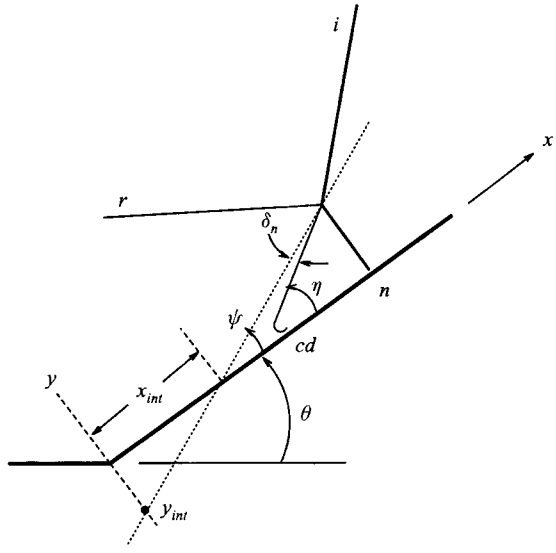

FIGURE 25. Relation between impact angle η, self-similar trajectory angle ψ and Mach-shock particle path deflection angle δ_n.

6. Conclusions

(1) When a strong shock propagating in a viscous, heat-conducting gas diffracts over a smooth rigid isothermal ramp with $\theta < \theta_e$, the effects of the properties of a real gas is to curve the shock triple-point trajectory and to delay the onset of the irregular (Mach) reflection. For $\theta < \theta_e$, the diffraction comprises a pre-cursor regular reflection which moves at a uniform speed along the ramp, is followed by a corner signal which is a sonic compression and eventually overtakes the pre-cursor also at a uniform speed and forces the eruption of a Mach shock. Even though $\theta < \theta_e$, the eruption occurs at, or near, the instant that the detachment condition is attained at the pre-cursor reflection point R. The Mach shock moves faster than the corner signal, and the unsteady system evolves into a self-similar complex Mach reflection. The interaction of the corner signal with the reflected shock causes it to bend smoothly into a stronger shock and produce a local irregularity analogous to a von Neumann reflection with the difference that the corner signal arrives at the interaction zone, whereas in a von Neumann reflection it leaves the zone.

(2) The properties of the corner signal with $\theta < \theta_e$, and before overtaking are as follows: it is a smooth isentropic compression; relative to it, the flow is supersonic on its upstream side and *sonic* on its downstream side; it is generally oblique to the flow, and unsteady; it is driven from the rear as though it were a shock detaching from a blunt body; the gradients across it may be substantial enough to be easily detected by schlieren apparatus.

(3) The assumption that the trajectory of the shock triple point is a straight line through the ramp apex (the parallax assumption) is wrong for a viscous, heat-conducting gas with isothermal and non-slip boundary conditions.

(4) There is strong, but not yet conclusive evidence that the criterion for the regular $\rightleftharpoons$ irregular transition of a self-similar, strong shock diffraction over a rigid ramp with isothermal and non-slip boundary conditions is the von Neumann criterion.

(5) The viscous, heat-conducting boundary layer is the dominant influence which reduces the self-similar rate of growth of the Mach shock as compared to an ideal gas.

We are indebted to Professor P. Colella for many conversations and for the use of his data in figures 16 and 18. Support for this work was provided by the Applied Mathematical Sciences Program and the HPCC Grand Challenge Program of the DOE Office of Mathematics, Information, and Computational Sciences under contract DE-AC03-76SF00098 and by the Defense Nuclear Agency under IACRO 93-817 and IACRO 94-831.

REFERENCES

ALMGREN, A. S., BELL, J. B., COLELLA, P. & HOWELL, L. H. 1993 An adaptive projection method for the incompressible Euler equations. In *Proc. 11th AIAA Computational Fluid Dynamics Conf. Orlando, Florida, July 6–9, 1993.*

AMES Research Staff 1953 Equations, tables, and charts for compressible flow. *NACA Rep.* 1135.

ANDERSON, D. A., TANNEHILL, J. C. & PLETCHER, R. H. 1984 *Computational Fluid Mechanics and Heat Transfer*. Hemisphere.

BELL, J. B., BERGER, M. J., SALTZMAN, J. S. & WELCOME, M. L. 1994 *SIAM J. Sci. Comput.* **15**, 127.

BEN-DOR, G. 1992 *Shock Wave Reflection Phenomena*. Springer.

BERGER, M. J. & COLELLA, P. 1989 *J. Comput. Phys.* **82**, 64.

BERGER, M. J. & OLIGER, J. 1984 *J. Comput. Phys.* **53**, 484.

BLEAKNEY, W. & TAUB, A. H. 1949 *Rev. Mod. Phys.* **21**, 584.

COLELLA, P. 1990 *J. Comput. Phys.* **87**, 171.

COLELLA, P. & HENDERSON, L. F. 1990 *J. Fluid Mech.* **213**, 71.

CRUTCHFIELD, W. Y. & WELCOME, M. L. 1993 *Scientific Programming* **2**, 145.

GLIMM, J., KLIPPENBERGER, C., MCBRYAN, O., PLOHR, B., SHARP, D. & YANIV, S. 1985 *Adv. Appl. Maths* **6**, 259.

HEILIG, W. H. 1969 *Phys. Fluids Suppl. I*, 154.

HENDERSON, L. F. 1987 *Z. Angew. Math. Mech.* **67**, 73.

HENDERSON, L. F. & LOZZI, A. 1975 *J. Fluid Mech.* **68**, 139.

HENDERSON, L. F. & LOZZI, A. 1979 *J. Fluid Mech.* **94**, 541.

HILSENRATH, J., HOGE, H. J., BECKETT, C. W., MASI, J. F., BENEDICT, W. S., NUTTAL, R. L., FANO, L., TOULOUKIAN, Y. S. & WOOLLEY, H. W. 1960 *Tables of Thermodynamic and Transport Properties*. Pergamon.

HORNUNG, H. G. 1986 *Ann. Rev. Fluid Mech.* **18**, 33.

HORNUNG, H. G., OERTEL, H. & SANDEMAN, R. J. 1979 *J. Fluid Mech.* **123**, 155.

HORNUNG, H. G. & ROBINSON, M. H. 1982 *J. Fluid Mech.* **123**, 155.

JONES, D. M., MARTIN, P. M. & THORNHILL, C. K. 1951 *Proc. R. Soc. Lond.* A **209**, 238.

KAWAMURA, R. & SAITO, H. 1956 *J. Phys. Soc. Japan* **11**, 584.

LOCK, G. D. & DEWEY, J. M. 1989 *Exps. Fluids* **7**, 289.

MARK, H. 1958 *NACA TM* 1418.

MIRELS, H. 1956 *NACA TN* **37**, 12.

MIRELS, H. & HAMMAN, J. 1962 *Phys. Fluids* **5**, 91.

MÖLDER, S. 1971 *CASI Trans.* **4**, 73.

NEUMANN, J. VON 1963 *Collected Works*, Vol. 6. Pergamon.

PANTAZAPOL, D., BELLET, J. C. & SOUSTRE, J. 1972 *C. R. Acad. Sci. Paris* **275**, A225.

PEMBER, R. B., BELL, J. B., COLELLA, P., CRUTCHFIELD, W. Y. & WELCOME, M. L. 1995 *J. Comput. Phys.* **120**, 278.

SEILER, F. & SCHMIDT, B. 1978 *11th Symp. on Rarefied Gas Dynamics, Cannes France* (ed. R. Campargue), p. 313. Commissariat a l'Energie Atomique.

SMITH, W. R. 1959 *Phys. Fluids* **2**, 179.

STEINTHORSSON, E., MODIANO, D. & COLELLA, P. 1994 Computations of unsteady viscous flows using solution adaptive mesh refinement in curvilinear body-fitted grid systems *AIAA*-94-2330. Also *ICOMP*-94-17, *NASA TM* 106704.

STEINTHORSSON, E., MODIANO, D., CRUTCHFIELD, W. Y., BELL, J. B. & COLELLA, P. 1995 An adaptive semi-implicit scheme for simulations of unsteady viscous compressible flows *Proc. 12th AIAA Computational Fluid Dynamics Conference, AIAA*-95-1727.

STERNBERG, J. 1959 *Phys. Fluids* **2**, 179.

VIRGONA, R. J. 1993 Shock wave diffraction. PhD thesis, University of Sydney.

WALENTA, Z. A. 1987 *Proc. 16th Intl. Symp. on Shock Tubes and Waves*, Aachen Germany (ed. H. Grõnig), p. 534. VCH Verlagsgesellchaft mbH.

ZELDOVICH, YA & RAIZER, YU 1966 *Physics of Shock Waves and High Temperature Hydrodynamic Phenomena*, p. 678. Academic.